An Encounter with the Ion and Electron Diffusion Regions at a Flapping and Twisted Tail Current Sheet

C. J. Farrugia[1], A. J. Rogers[1], R. B. Torbert[1], K. J. Genestreti[2], T. K. M. Nakamura[3], B. Lavraud,[4], P. Montag[5], J. Egedal[5], D. Payne[1], A. Keesee[1], N. Ahmadi[6], R. Ergun[6], P. Reiff[2], M. Argall[1], H. Matsui[1], L. B. Wilson III[7], N. Lugaz[1], J. L. Burch[2], C. T. Russell[8], S. A. Fuselier[2,9], and I. Dors[1].

[1]Dept of Physics and Astronomy and Space Science Center, University of New Hampshire, Durham, NH
[2]Southwest Research Institute, Durham, NH
[3]Institute of Physics, University of Graz, Graz, Austria
[4]Institut de Recherche en Astrophysique et Planetologie, Universite, de Toulouse, Toulouse, France
[5]University of Wisconsin-Madison, Madison, Wisconsin
[6]University of Colorado LASP, Boulder, CO
[7]NASA Goddard Space Flight Center, Greenbelt, MD
[8]Dept of Earth and Space Sciences, University of California, LA
[9]University of Texas at San Antonio, San Antonio, TX

Key Points:

- We analyze signatures of asymmetric reconnection earthward of the X-line in a flapping and reconnecting magnetotail current sheet.
- PIC simulations support MMS key observations and inferences.
- The flapping episode was associated with a substorm onset.

Corresponding author: C. J. Farrugia, `charlie.farrugia@unh.edu`

Abstract

We analyze data returned by the Magnetospheric Multiscale mission (MMS) constellation during a rapid ($\sim$ 1.5 s) traversal of a flapping and reconnecting current sheet (CS) in the near-Earth magnetotail (X $\sim$ -20 R_E). The CS was highly tilted, with its normal pointing strongly duskward. Its extreme thinness was confirmed by a curvature analysis of the magnetic field lines. The event was associated with a guide field of 8% of the reconnecting components. From the pitch angle distributions of low-energy electrons we infer that the crossing occurred earthward of the X-line. Traveling practically normal to the CS, MMS encountered an ion diffusion region (IDR) in which was embedded an electron diffusion region (EDR). IDR signatures included breaking of the ion frozen-in condition in the presence of Hall **B** and **E** fields. EDR signatures included a strong out-of-plane current associated with a super-Alfvénic electron jet, evidence of positive energy transfer, and a temperature anisotropy ($Te_{\|} > Te_{\perp}$) which disappeared at the field reversal. Derived scale sizes normal to the CS are: $\sim$6.9 d_e (EDR) and $\sim$0.4 d_i (IDR) (40 and 100 km). **We estimate the average dimensionless reconnection rate as 0.077 $\pm$ 0.050**. The observations and inferences are supported by PIC numerical simulations. **We find very good agreement in the reconnection rates.** We also discuss the effects of asymmetries in the density, temperature and magnetic field strength on the Hall fields and length of the outflow jets. The event is associated with a substorm onset which began 7 min after the MMS observations.

1 Introduction

Soon after the discovery of the geomagnetic tail at the start of the space age (Ness, 1965), it was found that the tail can sometimes move rapidly in a north-south direction (Speiser and Ness, 1967). This flapping motion was deduced from a reversal in the polarity of the Earth-Sun component of geomagnetic tail field, B_x, concomitant with a decrease in the total magnetic field strength. The typical duration of this up-down motion is a couple of minutes, with an amplitude of a few R_E (Toichi and Miyazaki, 1976, Sergeev et al., 2003, Runov et al., 2009). Tail flapping is now a well-known phenomenon that has been repeatedly reported by spacecraft making observations close to the tail current sheet (CS, or neutral sheet NS) in the near-tail region (R $\sim$-15 to -30 R_E). Not well established is what gives rise to it. Over the years both internal (see e.g. Sergeev et al., 2004, Zhang et al., 2005) as well as external (i.e. solar wind origin; e.g., Toicki and Miyazaki (1976), Sergeev et al., 2008, Runov et al., 2009) origins have been proposed.

It was Lui et al. (1978) who first pointed out that in tail flapping we are dealing with a wave propagating from the center of the tail towards the flanks. This was inferred from the polarity changes in the east-west component of the field, B_y: these changes reverse in adjacent crossings of the CS. Our understanding of tail flapping was fostered by multi-spacecraft observations made, in particular, by Cluster and THEMIS. In a number of papers (e.g. Zhang et al., 2002, 2005, Runov et al., 2003, 2005, Sergeev et al., 2003, 2004, see also Shen et al., 2008 and references therein) the properties of this wavy motion were investigated. It was proposed that during tail flapping a kink-like disturbance propagates east-west towards the flanks (Sergeev et al., 2003, 2004). The vertical speed of the CS along its normal was calculated to be 60-100 km/s or more (Runov et al., 2003; Sergeev et al., 2004). The flankwise speed of the wave was estimated to be a few tens of km/s (Runov et al. 2009). A statistical analysis (Runov et al., 2005) yielded a current density of 5-25 nA/m^2 . Sometimes the cross-tail current was also bifurcated, being concentrated in two sheets with a weak magnetic field in between (e.g. Runov et al., 2003).

One complication is that the tail current sheet can be locally twisted, with its normal not pointing in the z-direction of the Geocentric Solar Magnetospheric (GSM) coordinate system. Further, this tilt can be quite large, with the CS-normal locally pointing mainly in the east-west direction. In this case, the wavy motion due to flapping would be superposed on an extremely-twisted CS (e.g. Zhang et al., 2002, Sergeev et al., 2003).

A note on the possible generating mechanisms is in order. Among the possible origins of tail flapping is that of solar wind Alfvénic waves when the total field is bigger than 10 nT and which propagate down the tail with the solar wind. They modulate the tail magnetopause boundary, which is then reflected in CS oscillations. This was proposed by Toichi and Miyazaki (1976). After that the main view was that the origin is internal to the tail, though nothing was nailed down conclusively. However, the possibility of a solar wind origin was raised again in Sergeev et al. (2008) and Runov et al. (2009), in particular, the effects of directional changes in the z-component of the solar wind flow. This will be of great relevance here.

Another mechanism was proposed by Erkaev et al. (2008), consisting of a new MHD, 'double-gradient' wave model. The theory requires the simultaneous presence of a gradient of the transverse magnetic field (B_x) along the normal (z) and of the normal magnetic field component (B_z) along the transverse (x) directions with respect to the CS. Stable flapping motion requires that the product of these two gradients be positive.

We know, of course, that magnetic reconnection can take place in the geomagnetic tail. Here, magnetic field lines which have been opened during reconnection on the dayside are closed again and returned back to the dayside, thus giving rise to a twin-cell plasma circulation pattern and forestalling wholesale erosion of the dayside magnetosphere. The first clear evidence of an ion diffusion region during tail reconnection was given by **Nagai et al. (2001)**. This is consistent with collisionless reconnection.

With this background, one would then expect tail reconnection to occasionally happen during tail flapping. This is the situation we focus on here. We discuss MMS data in the near-tail region (X $\sim -20R_E$). We have, namely, a series of tail current sheet flapping motions lasting about 24 min where in one instance all the spacecraft traverse the CS very rapidly ($\sim$1-2 s), implying a very thin CS. In fact we find it was thin enough for ions and electrons to both decouple from the magnetic field. Various reconnection signatures, such as super-Alfvénic electron flow jets in the in-plane and out-of-plane directions, energy transfer in the electron frame, Hall electric and magnetic field signatures, etc., are seen during the traversal. The brevity of the CS-passage implies very curved magnetic field lines associated with a thin CS. Its structure can be examined using differential geometry methods applied to the magnetic field lines and based on the 4-spacecraft MMS configuration. It also implies the possibility of departure from adiabatic motion, when the gyroradii of the particles become of order of, or larger than, the curvature radius of the magnetic field lines (MFLs). In this event the MMS spacecraft do not observe any flow reversals, since they cross on one side of the X-line. We shall also argue that the EDR is crossed earthward of the X-line during this episode, thus providing one of the few published examples of reconnection on one side of the X-line. PIC simulations are also presented and they support this interpretation of the event. **They also suggest a reconnection process which is steady and occurring at a rate consistent with that inferred from the observations.**

The layout of the paper is as follows. We first give an overview of the longer flapping interval, highlighting typical time and length scales, and augmenting it with an analysis of the field line curvature. We then discuss the electron behavior in our 10-s long interval of interest. After that, we give the observational evidence for the presence of an EDR embedded in an IDR and of the claim that the MMS spacecraft are crossing the EDR in an approximately normal direction and earthward of the X-line. A section follows where we present the results of PIC simulations done with initial conditions tailored to fit the event. In the discussion we suggest a likely cause of the flapping motions and also consider the effect of plasma and field asymmetries on the structure of the reconnection region. We finish with a short summary.

2 Instrumentation

The MMS spacecraft measure electric and magnetic fields using the FIELDS instrument suite, which consists of three electric field and three magnetic field instruments (Torbert et al., 2016). The analog and digital fluxgate magnetometers (AFG/DFG) measure magnetic fields in the frequency range from DC up to 64 Hz (Russell et al., 2016). The higher frequency range, from 1 Hz up to 6 kHz, is covered by a search-coil magnetometer (SCM; Le Contel et al., 2016). Level 2 fluxgate magnetometer (FGM) data of version 5.86 and higher (highest available as of submission) were used throughout this study.

The Electric Field Double Probe (EDP) components of the FIELDS suite return measurements of the electric field at each spacecraft. The two pairs of spin-plane (SDP) and axial (ADP) double probes allow MMS to make direct measurements of the full 3D electric field, ranging from DC to 100 kHz (Lindqvist et al., 2016, Ergun et al., 2016). These data are combined into the EDP data product for 3D vector $\mathbf{E}$ measurements. Version 3.0.0 of the level 2 EDP data products was used throughout this study. Level 2 burst mode data was used unless stated otherwise. Level 3 (L3) EDP data were used in some parts of the analysis and were produced specifically for this study. L3 EDP data features reduced uncertainty derived from careful examination and tailoring of the filters used to correct for periodic gain variations and interference from other instruments. This requires extensive investigation of the spacecraft status and local environment at the time of measurement, so that intervals of L3 EDP data are generated only on request to the FIELDS team.

The Fast Plasma Instrument (FPI) on MMS returns high cadence electron and ion distributions in the energy/charge range from 10 eV/q to 30 keV/q. Each MMS satellite is equipped with eight FPI spectrometers which, when combined with electrostatic control of the field-of-view, allows FPI to sample the full electron and ion distributions (Pollock et al. 2016). The core ion distributions may extend beyond the range of FPI, so that actual ion temperatures may be higher than what is calculated using FPI moment data. Level 2 FPI ion moments of version 3.3.0 were used throughout this study.

Positions of the individual spacecraft in the MMS fleet are provided using Magnetic Ephemeris and Coordinates (MEC) data products (Morley, 2015) and are calculated using the LANLGeoMag suite (Henderson et al. 2018). In order to ensure that the formation of the MMS fleet was appropriate for the calculation of spatial gradients, a minimum value of the Tetrahedron Quality Factor (TQF: Fuselier et al. 2016) was required with $TQF \geq 0.8$. All instrument data used in this study are available from the MMS Science Data Center (https://lasp.colorado.edu/mms/sdc). Level 2 burst mode data was used throughout this study except where explicitly noted. Calculations of the magnetic field line curvature and curlometer current density were made using the mms-curvature library and is publicly available (https://github.com/unh-mms-rogers/mms-curvature).

Interplanetary data are from *Wind*. The magnetic field (Lepping et al., 1995) and the plasma data from the 3DP instrument (Lin et al., 1995) are at 3s resolution. The geomagnetic indices are obtained from NASA/OMNI data website, and the geomagnetic field data are from the SuperMag website.

3 Observations

3.1 Overview

By way of an overview, Fig 1 shows magnetic field observations made by MMS1 during the 40-min interval from 20:10:00 to 20:50:00 UT, June 17, 2017. The first three panels show the components of the magnetic field in GSM coordinates, followed by the total field strength. The MMS satellites are located in the near-tail at X $\approx$ -20 R_E and on the dawnside (Y$\approx$ -10 R_E). The polarity changes in the B_x component provide clear evidence of tail current sheet flapping, and four clear instances may be discerned. The opposite sense of B_y polarity reversals at adjacent current sheet (CS) crossings indicate that the associated waves move toward the flanks (Lui et al., 1978). Typically, each crossing lasts from a few tens of sec to a couple of min.

An exception to this occurs at $\sim$20:24 UT (arrowed). Here the CS crossing is very brief, and it took MMS only $\sim$1.5 s to go from one side to the other. This implies (a) that it is a very thin CS, and (b) that there is more to this crossing than just a flapping. We shall show below it is a crossing through the EDR of a reconnecting CS. Note that minimum B is not quite 0 nT, so there is a small guide field (see below).

Fig 2 shows the MFL curvature and angle relative to the current sheet in the region. For reference, the average magnitude of the magnetic field across all four spacecraft is shown in panel a. The MFL curvature is defined as $\mathbf{K} = \mathbf{b} \cdot \nabla \mathbf{b}$, where $\mathbf{b}$ is the unit vector along the field line. It is computed using magnetic field and positional data from the four spacecraft. The encountered X-line was embedded in the second of four consecutive neutral sheet crossings.

The calculated radius of curvature (panel c) is never smaller than half the spacecraft separation, indicated by the horizontal dashed purple line. The MFL radii of curvature during each of these crossings show a compression of the CS evolving over successive encounters. The first crossing shows a current sheet compressed broadly to near electron scales. The second encounter contains the X-line which is the focus of our study here and displays the thinnest current sheet, indicated by having the smallest radius of curvature of the observed crossings. Later crossings have progressively larger radii of curvature, so that the current sheet in the neighborhood of MMS thickened after the X-line encounter.

Calculating the tilt angle (γ_N) between the current density and the normal to the osculating plane of the magnetic field lines (Shen et al. 2007, 2008), we find that the CS tilt increased as its thickness decreased (panel d). The first flapping CS encounter shows a small tilt angle ($< 30°$) while the tilt seen at 20:24:07 UT during the second CS encounter is significantly larger ($\sim 80°$). In the subsequent CS encounters, the tilt angle reduces progressively to smaller values as the greater flapping event dies down.

3.2 Electron Behavior

We now switch to a coordinate system, LMN, centered on the CS. Carrying out a minimum variance analysis (MVAB) on the magnetic field data (Sonnerup and Scheible, 1998) over the interval 20:24:05 – 20:24:10 UT, we obtain: $\mathbf{L}$ = (0.930, 0.296, -0.216), $\mathbf{M}$ = (-0.275, 0.176, -0.945), and $\mathbf{N}$ = (-0.242, 0.938, 0.245) in GSM coordinates. The intermediate-to-minimum eigenvalue ratio = 15.9, i.e. large enough for the result to be robust. The normal $\mathbf{N}$ is mostly in the positive GSM Y-direction, i.e. pointing towards dusk. So we have a flapping CS which, in addition, is strongly tilted in the YZ plane.

To check how reliable this LMN system is, we need to obtain $\mathbf{N}$ independently, for example, by triangulating a feature seen at different times by all four spacecraft (Russell et al., 1983; Knetter et al., 2004). In Fig 3 we plot on the right the profile of B_z over a 2-s period when it goes from positive to negative values. We can see that the traces of MMS2 and MMS4 (red and blue) are indistinguishable because these two spacecraft cross the CS practically simultaneously. Their separation vector when they are crossing is $\mathbf{D}_{2,4}$ = (21.8, 6.3, -11.0) R_E. This makes an angle of 91° with the MVAB $\mathbf{N}$, which is consistent with the previous result for $\mathbf{N}$, and implies also that there is no local warping.

The separations of the spacecraft relative to the first one to cross the CS, i.e. MMS3 (green), are shown in the left panels of Fig 3. The average spacecraft separation is about 26 km. At 20:24 UT, MMS3 is at (-19.3, -10.3, 5.5) R_E (GSE). The wave associated with the flapping moves from MMS3–to–MMS2/MMS4–to–MMS1, advancing towards dawn, as it should (see Introduction). It took ∼0.5 s to go from MMS3 to MMS1, separated mainly in the Y-direction by ∼25 km, so the speed toward the flanks is ∼50 km/s.

We now consider the MFL curvature during the second encounter, the one of interest here. In Fig 4 we plot the curvature parameter (also called "adiabaticity parameter") $\kappa \equiv (R_c/R_{ge})^{1/2}$ evaluated at the barycenter of the MMS configuration, where R_c is the radius of curvature of the MFLs, and $R_{g,e}$ is the gyroradius of electrons of perpendicular energy 200 eV, 1 keV and 5 keV, respectively, distinguished by colors. At around 20:24:07 UT, $\kappa < 1$ and the maximum gyroradii are larger than the minimum radius of curvature of the MFL. This implies a very thin CS where the electrons are no longer coupled to the magnetic field and their motion is non-adiabatic. The electrons are scattered for $\kappa < 3$ (**horizontal line**, Egedal et al., 2008; Lavraud et al., 2016), and become chaotic for $\kappa < 10$ (Büchner and Zelenyi, 1989).

Fig 5 displays features of the electron behavior over an 8-s interval centered around the CS crossing. For reference, the first two panels show the magnetic field components in LMN coordinates, and the field strength. In anticipation of results given below, the vertical guidelines bracket the IDR (orange) and EDR (green). We note the following: (i) there are asymmetries across the CS in B, Ne and Te. Before the CS crossing the electrons are more dense, hotter, and lie in a somewhat weaker magnetic field; (ii) There is a strong electron jet peaking at $\sim$2200 km/s, which is mainly in the out-of-plane M-direction (panel 6). With an inflow Alfvén speed, $V_{A,in}$ $\sim$400 km/s, it is super-Alfvénic with M_A $\sim$ 5.5; (iii) There is a flow reversal in the L component (panel 5) just after 20:24:08.2 UT, as MMS1 approaches the separatrix on leaving the EDR. This reversal is due to the dominant amount of low-energy electrons entering the EDR along the separatrix as well as the deceleration of the higher energy exhaust electrons, both due to a possible ambipolar electric field, E_L (blue trace in panel 5). This aspect of the EDR dynamics is the subject of future work.

We note that the density asymmetry, of about 25%, as well as the asymmetry in B and Te, have a significant effect on the length of the outflow jets (Montag, 2018, Montag et al., 2020). They also affect the temporal profile of the Hall fields. We return to these points in the discussion section.

The event exhibits no reconnection-related ion or electron flow reversals (see Fig 5 for the electrons and Fig 9, below, for the protons), i.e. the X-line does not pass over the spacecraft. On which side of the X-line are the spacecraft crossing the CS? Fig 6 shows the pitch angle distributions (PADs) of low-energy electrons (20-200 eV) in the order from top to bottom MMS 3-2-1, i.e. moving dawnward. Before the CS crossing (when $B_L <$ 0) the flow is parallel to $\mathbf{B}$, while after (when $B_L > 0$) it is anti-parallel to $\mathbf{B}$. This behavior indicates that MMS is crossing the CS earthward of the X-line (see e.g. Wang et al., 2010, their Fig 3). In this way the low-energy electrons are aligned with the magnetic field and moving towards the X-line on both sides of the CS.

3.3 An EDR embedded in an IDR

In this event the MMS constellation crossed both the IDR as well as the EDR. We now discuss the identification of these diffusion regions, starting with the IDR. Fig 7 shows from top to bottom, the adiabatic expansion parameter, δ_i (Scudder et al., 2008), the current density in the out-of-plane (M) direction, the electric field normal to the CS, E_N, and the out-of-plane magnetic field, B_M. The dotted red line in the last panel is the guide field, B_g (=-0.8 nT), calculated from the angle between the ambient reconnecting fields. Parameter δ_i in panel 1 is the ratio of the $\mathbf{E}_{\perp}$-to-magnetic forces experienced by an ion. A value ≥ 1 is a good indication of demagnetized ions.

The normal electric field is the Hall **E**-field, produced by the differential motion of ions and electrons. It is strong and it points to the CS from both sides. E_N pointing to the CS from both sides is consistent with reconnection under only a small guide field (see Torbert et al. 2018, and references therein.) E_N is also asymmetric, with the negative part being stronger, a feature we return to **when we compare with the PIC simulations** and in the Discussion. The Hall magnetic field, $B_H = B_M - B_g$ goes from negative to positive, as appropriate for a crossing earthward of the X-line. In this case, positive B_H is stronger. Parameter J_M gives an estimate of the duration of the IDR encounter (Zhao et al., 2019), which is shown bracketed by the vertical orange lines. To further support this extent of the IDR we show in Fig 8 the quantity $\mathbf{E}\times\mathbf{B}/B^2$ in black and the perpendicular flow velocity of electrons (in blue) and ions (red). It is seen that within the boundaries shown in Fig 7 the latter are not coupled to the magnetic field. The estimated thickness of the IDR in the normal direction can be obtained from the velocity of the CS along its normal (see below) and the duration of the crossing. We obtain $\sim$100 km, i.e. about 0.4 d_i.

Together with Fig 7, Figs 9 and 10 provide evidence of the presence of an EDR embedded within the IDR. Fig 9 shows the L (red), M (orange), and N (green) components of the magnetic field for reference, the proton velocity components (in black, the total velocity), and **proton temperatures in eV**, the electron velocities parallel (red) and perpendicular to **B**, the parallel (red) and perpendicular electron temperatures in eV, the L3 electric field parallel to **B**, with error bars included, **and the out-of-plane component of the electric field,** E_M.

The proton data show a lack of any ion outflow jetting (in L direction). This is consistent with a spacecraft trajectory which crosses the EDR close to the X-line. **The proton temperatures show no evidence of heating.** The electron temperatures are generally unequal with $Te_{\|} > Te_{\perp}$, an anisotropy which is more pronounced before the CS crossing. The anisotropy goes away around $B_L \sim 0$ in the time from 7 to 7.8 s. As the spacecraft cross the DRs, the $Te_{\perp}$ increases, implying that energy is going not only to produce the electron jets but also to heat the electrons perpendicular to $\mathbf{B}$ (see also Torbert et al., 2018). The rise is from 500 to 640 eV, i.e. about 28%. The electron velocities show a prominent field-aligned flow (red trace) at the CS crossing. Away from it, the perpendicular velocities dominate. When the electrons exit the EDR, their parallel flow reverses direction, an effect caused by $E_{\|}$.

We now consider some relevant scale sizes. The separation vector between MMS1 and MMS3 as they cross the CS is $\mathbf{\Delta}(1,3)$ = (-4.60, 23.11, 15.0) km. This vector makes an angle of 18.5° with the CS normal (see above), so their separation along $\mathbf{N}$ is 26.5 km. It took 0.42 s for the CS to go from MMS3 to MMS1, so the speed of the CS along its normal is -63.1 km/s. Compared to quoted values, this is a fairly typical one (see e.g. Runov et al., 2003, Sergeev et al., 2003). The spacecraft took 1.52 s to cross the IDR and 0.75 s to cross the EDR in the normal direction. Thus the normal width of the EDR = 44.2 km, i.e. 6.9 d_e (electron inertial length). To further confirm this, we use Ampere's law. Across the EDR $\Delta B_L \sim 12$ nT and $J_M \sim 200$ nA/m^2. This yields Δ_N (EDR) = 48 km, consistent with the previous estimate. Further, using the minimum radius of curvature as an estimate for maximum half-width of the CS (Shen et al. 2008), $h \leq R_{C,min} = 22.0km$ implying a width of $\leq 44.0km$ for the CS near the X-line.

In the EDR, a clear electric field parallel to $\mathbf{B}$ is seen. A careful and rigorous analysis over a 20-s interval gave an error bar of 1.12 mV/m on the L3 values, which has been overlaid. Thus, the $E_{\|}$ is real. **We now use the electric field measurements to estimate the reconnection rate.**

The reconnection electric field E_R is evaluated as E_M in the velocity frame co-moving with the X-line, i.e., $E_R = \langle E_M + (\mathbf{V}_{Xline} \times \mathbf{B})_M \rangle$. When calculating E_R, errors may arise from improper assessments of the orientation and velocity of the X-line. If the X-line orientation is improperly determined, then the very large E_N may contribute to the much smaller E_M (see for instance

Genestreti et al. 2018, their Fig 5c-d). Given that this is a crossing roughly normal to the CS, the largest source of error resulting from improper assessment of the X-line velocity will be $B_L V_N$. Following Genestreti et al., we have determined the correlation between E_M and E_N in the X-line frame, noting that a strong correlation may indicate coordinate errors. (Results are summarized in Supplementary SFig 1.) We find nearly no correlation and a least-squares fit of E_N vs E_M has a slope of 0.018 $\pm$ 0.008 (middle panel), corresponding to an error of 1.0° $\pm$ 0.5° in our coordinate axes, which confirms that our coordinate system is robust. (For comparison, the robust coordinates of Genestreti et al.'s Fig 5d had an error of $\sim 1.3^\circ$).

The reconnection electric field is determined as the average of E_R within the EDR interval (20:24:07 – 20:24:07.8 UT). We use E-field data from all four spacecraft, smooth the data using a 3rd-order Savitzky-Golay filter and a $\pm$0.05 second convolution window, and exclude points with large $|E_N| >$5 mV m^{-1}. The slopes of the fit lines, shown in SFig 1, are used to rotate our LMN coordinate system before calculating E_R. The rotation angles are very small, being $\leq 1.7^\circ$, and this correction therefore has a very minor impact ($\leq 4.5\%$) on E_R. The result is E_R = 0.442 $\pm$ 0.281 mV/m. To obtain the normalized reconnection rate, we choose an inflow interval from 20:24:10-20:24:11 UT, which is steady, and divide E_R by the product of the inflow upstream Alfvén speed (V_{Ai0}) and inflow magnetic field strength (B_{L0}). The resulting dimensionless rate is $E_R/V_{Ai0}B_{L0}$ = 0.077 $\pm$ 0.050.

This calculation was done using our nominal estimate for the X-line speed in the normal direction, derived above, i.e. V_N = 63 km/s. We consider now the impact of uncertainties in V_N of $\pm$20 km/s ($\pm$30%) (top and bottom panels). For V_N = 40 km/s we use the same approach to obtain $E_R/V_{Ai0}B_{L0}$ = 0.078 $\pm$ 0.050 and the least-squares fit of E_N vs E_M has a slope of 0.11° $\pm$ 0.46°. For V_N = 80 km/s we find $E_R/V_{Ai0}B_{L0}$ = 0.076 $\pm$ 0.050 and a slope of 1.7° $\pm$ 0.5°. We conclude that the dimensionless reconnection rate is ~ 0.077, though with uncertainty bars of order of $\pm$ 60% which are predominantly a result of scatter in E_M. In section 4 this result is compared with that obtained from PIC simulations.

Further EDR properties are shown in Fig 10. Panels 3 and 4 give the parallel and perpendicular current densities. In the center of the EDR the current is primarily in the parallel direction and generated by electrons moving anti-parallel to the field. At the edges of the EDR it is primarily in the perpendicular direction. The current densities are very strong: a couple of hundreds nA/m^2 (Fig 10 panels 3 and 4). Compare these with the values of a few tens of nA/m^2 resulting from the statistical survey of Runov et al. (2005) (see Introduction). Fig 11 shows the PADs of low-, mid- (200 eV - 2 keV), and high-energy (2 - 30 keV) electrons. Mid-energy electron PADs show a 'hole' in the **anti-**parallel direction while the higher energy electrons are isotropic.

Fig 10, panel 5 shows the energy transfer term **J**.**E**', where **E**' is the (L3) electric field (sampling rate of 654 Hz) in the electron rest frame ($\mathbf{E}' = \mathbf{E}+\mathbf{V_e}\times\mathbf{B}$). The central EDR is a load region where energy is transferred from electromagnetic fields to particles. At its edges, roughly between the IDR and EDR boundaries, we have generator regions, with the electrons feeding energy to the magnetic field. Interestingly, while positive energy transfer is a good signature of an EDR, the largest, positive energy transfer occurs outside the diffusion regions, north of the CS. This is where the electric field component E_L is acting on low-energy electrons entering the EDR along the separatrices and on the higher energy exhaust electrons, decelerating them. The electron Mach number $Ve/V_{Te_\perp}$ is ~0.15.

4 PIC Simulations

4.1 Simulation Setup

We performed 2-1/2 dimensional simulations of this MMS event, using the fully kinetic particle-in-cell code VPIC (Bowers et al., 2008). The simulation is performed in the XZ plane and is started from a simple 1-D Harris type current sheet with a weak guide field. The initial magnetic field and the corresponding number density are set up as $B_x(z) = B_0 tanh(z/L_0)$, $B_y = B_g$, and $n_{i,e}(z) = n_0 sech^2(z/L_0) + n_b$, where B_0 is the background reconnecting magnetic field component, B_g is the initial, uniform guide field, n_0 is the Harris density component, n_b is the background density, and L_0 is the half-thickness of the initial CS. The initial parameters are set up by referring to the observed values as n_0/n_b =1.25, T_i/T_e =6.25, and $B_g = -0.08B_0$. The ion and electron temperatures are set to be uniform. L_0 is set to be 0.6 d_i, where d_i is the ion inertial length based on n_0. The ratio between the electron plasma frequency and the gyrofrequency is set to be ω_{pe}/Ω_e =2.0. The ion-to-electron mass ratio is m_i/m_e =100. The system size based on d_{i0} is set to be $L_x \times L_z = 80d_i \times 40d_i = 800d_e \times 400d_e = 7680 \times 3860$ cells with a total of 1.2×10^{11} superparticles (4000 particles/cell on average). The boundary conditions are periodic along the x-direction, with conducting walls along the z-direction. A weak initial magnetic field perturbation is added at the center of the simulation domain according to $\delta\mathbf{B} = \mathbf{z} \times \nabla\mathbf{\Phi}$, where $\Phi = 0.02B_0 sin(x/L_x)cos(z/L_z)$, such that reconnection starts near the center of the simulation domain x=0.

4.2 Results

Fig 12 shows an overview of the simulation results. As seen in past kinetic simulations of reconnection with no or weak guide field, the typical Hall signatures are seen near the X-point; the quadrupolar B_y pattern due to the Hall currents (Fig 12a) and the polarization Hall electric field E_z pointing toward the current sheet center due to the charge separation (Fig 12b). The strong U_{ey} peak, which dominantly sustains the out-of-plane current component, is seen near the X-line, indicating the location of the IDR.

To compare these simulation results with the MMS observations, we performed virtual observations along the virtual probe path shown in Fig 12. Here the path is chosen by (i) determining the z=0 point with a similar $|U_{ey}/V_{Ae}|$ to the observed $|U_{ey}/V_{Ae}| \sim 0.15$, corresponding to $|U_{ey}| \sim 2500$ km/s where $V_{Ae} \sim 1.7 \times 10^4$ km/s based on n $\sim$ 0.5 cm^{-3} and $B_0 \sim 12$ nT), and then (ii) setting the angle from the z-axis in the x-y plane as large as the observation ($\sim$18°). The path crosses the region on the earthward side of the EDR, where the Hall signatures are strongly seen.

Fig 13 shows the virtual observation results. We see the moderate U_{ex} (corresponding to the outflow jet) and strong U_{ey} (corresponding to the out-of-plane current) enhancements near the current sheet center (Fig 13b) sandwiched by the negative-to-positive Hall B_x variation (Fig 13a) and the positive-to-negative Hall E_z variation (Fig 13c). The temperature anisotropy, with $Te_\parallel > Te_\perp$, is present except near the current sheet center, that is, in the EDR (see Fig 13d). This could be due to adiabatically trapped inflowing electrons and the resulting energization by the ambipolar parallel electric field as predicted in past kinetic studies (e.g., Egedal et al., 2013; Le et al., 2016).

These variation patterns are very similar to those seen in the observations (see Figs 5 and 7). **(SFig2 collects these various observational parameters into one plot.)** In particular, **(i)** the asymmetry in the magnitudes of the positive and negative B_y peaks (compare Fig 13a and Fig 5, panel 1), **(ii)** the flat interval seen near the U_{ey} peak (compare Fig 13b and Fig 5, panel 7) and **(iii)** the asymmetric E_z profile (compare Fig 13 c with Fig 7, panel 3) show consistency between the simulation and observations. In addition, when taking the normalization parameters as $B_0 \sim 12$nT, $n \sim 0.5$ cm^{-3}, and $V_{Ae} \sim 1.7 \times 10^4$ km/s, the peak values of B_y, U_{ex}, U_{ey} and E_z variations seen in the simulation are calculated as about 2.5 nT, 1000 km/s, 2500 km/s and 8 mV/m, all of which are in reasonable agreement with the observations (see Figs 5 and 7). **These consistencies indicate that the 2-1/2 D geometry on which the simulations are based is a good representation of reality.**

We now calculate the dimensionless reconnection rate resulting from the simulations. Fig 14 shows the evolution in time of this quantity. After reconnection onset at T $\sim$ 10 Ω_i^{-1}, the reconnection rate rapidly increases. After T $\sim$35 Ω_i^{-1}, it saturates to a value of about 0.085. This is in very good agreement with the (average) rate deduced from observations, i.e. R = 0.077 $\pm$ 0.050. The time in the simulation, at which the simulation results are compared with the MMS data, is in a nearly steady phase of reconnection (i.e. with nearly constant reconnection rate) as shown. In addition, the consistencies indicate not only that the reconnection signatures seen in the 2.5 D simulation really occurred in this MMS event, but also that the observed reconnection process was in a nearly steady phase

5 Elements of Geoeffects

We now examine some geomagnetic perturbations during this event, in particular, substorm activity. From 17 to 23 UT no geomagnetic storms and only one substorm were recorded (source: OMNI database). Fig 15a (left) shows the north-south (X) component of the geomagnetic field at six stations of the IMAGE magnetometer chain. The stations are located (from top to bottom) at corrected geomagnetic latitudes 67.7 to 66°. In our time of interest ($\sim$20:30 UT), the magnetometer chain was at $\sim$23 MLT. This is an ideal location to monitor substorm activity (Akasofu, 1964, Wang et al., 2005). In an earlier paper, Rogers et al. (2019) found a clear preference for the occurrence frequency of geomagnetic tail IDRs to also peak at this MLT sector.

The decrease in the X-component (Fig 15a) recorded by the stations at around 20:30 UT, i.e $\sim$ 6 min after the MMS crossing of the EDR, signifies the activation of the westward electrojet current (WEJ), which is the diversion of the dawn-dusk cross-tail current to the ionosphere during substorm onset. This being near summer solstice and a sunlit atmosphere, the electrojet signatures are weaker. Fig 15b (right) shows the auroral electrojet indices AE and AL and the polar cap-north index (PCN; Troshichev et al., 1998), a measure of the strength of magnetospheric plasma convection. At $\sim$ 20:30 UT a substorm onset is recorded by the auroral indices. Simultaneously, the PCN index gives an indication of enhanced plasma convection. Both dayside as well as nightside reconnection can contribute to increases in magnetospheric convection (Lockwood et al., 1990). Clearly, here the origin of this enhancement is tail reconnection.

6 Summary and Discussion

We first summarize our work. We have analyzed MMS data at the dawnside, near-tail of a flapping interval containing one very rapid crossing of the current sheet. We argued that this crossing was due to reconnection occurring in a very tilted and thin current sheet. Using level 3 electric field data, several signatures were found supporting the presence of an IDR and EDR. The pitch angle distributions of low-energy electrons argued in favor of an encounter on the earthward side of the X-line. The absence of ion jetting was ascribed to the proximity of the encounter to the X-line. Ours was a case of asymmetric reconnection (in B, Ne and Te) in the presence of a very-small (8%) guide field. **Comparison with 2.5 D PIC simulations reproduced various aspects of the observations, including asymmetries in the temporal profiles, and gave a good agreement in the reconnection rate.** We now discuss some points resulting from this work.

Attempts to understand this event have been made before, to which we draw the reader's attention. Huang et al. (2018) observed the ion behavior at the X-line discussed here and determined that it resulted from secondary reconnection between flux ropes in the outflow region of a distant primary X-line. While they note the strongly tilted boundary coordinate system, they do not investigate the implications of this in their analysis.

They suggest that the event is a case of reconnection on the electron scale. Wang et al (2018) discuss the tilted nature of the current sheet of interest and associate it with possible magnetotail flapping. Wang et al. (2018), however, conclude that the electron scale current sheet does not contain a reconnecting X-line. Although there is some overlap between our work and these two studies, there are also significant differences. We thus offer here an alternative interpretation to a very intriguing event.

As noted in the Introduction, a solar wind origin for tail flapping has not been ruled out. Two possibilities mentioned were: (a) Alfvén waves with a high field strength (of order 10 nT), and (b) directional changes in the Z component of the flow velocity, V_z. We now discuss these briefly in relation to our event.

We look first at *Wind* data for the longer period 16:20-22:00 UT. This is a fast solar wind flow and we can show that the field and flow fluctuations satisfy the relation $\Delta\mathbf{B}_\perp = (\mu_o\rho)^{1/2}\Delta\mathbf{V}_\perp$, with correlation coefficients of $\sim$0.8 (over 5015 data points) and slopes close to unity (shown in SFig 3). These fluctuations are thus Alfvénic. However, this long time interval contains no cases of tail flapping **aside from that** shown in Fig 1. So Alfvén waves are certainly not a sufficient condition for flapping to occur.

We now turn to deflections in the solar wind V_z component (e.g. Runov et al., 2009). Fig 16 shows solar wind data for the 1-hour interval 19:20 to 20:20 UT. In the third panel of the correlated field and flow fluctuations (first 3 panels) one can see clear deflections in V_z. This fast solar wind has otherwise stable plasma parameters, in particular, the dynamic and thermal pressures. During this interval, the *Wind* spacecraft was at (202.0, 21.9, -10.8) R_E, sufficiently close to the Sun-Earth line for its measurements to affect the magnetosphere. A minimum variance analysis of the magnetic field in the time interval 19:40 to 20:00 UT gives a plane with normal, $\mathbf{N}$ = (0.96, -0.25, -0.14) (GSM), i.e. inclined towards dawn at 76° to the Sun-Earth line. This structure will arrive at the dawnside magnetopause in an estimated 37 min, i.e. a few min before the episode of tail flapping shown in Fig 1 is observed by MMS. We thus conclude that this solar wind disturbance in the north-south (GSM) flow component is a very plausible cause of the tail flapping reported here.

During each of four successive encounters of MMS1 with the flapping current sheet, its half-thickness $h = R_{C,min}\cos(\gamma_N)$ was calculated from the minimum radius of MFL curvature and tilt angle of the current sheet at each encounter (Shen et al. 2008). These show a flapping current sheet thinning to near electron scales before the X-line encounter at 20:19:04 where $h \approx 40km$, and slowly thickening in later encounters with half-thicknesses in the hundreds of km after the X-line. In each of these encounters the current sheet thickness is well below ion scales and some Hall effect from demagnetized ions is expected. The magnitude of the out-of-plane (i.e. M) curvature vector, (Fig 17, panel c)) follows the out-of-plane component of the current density (J_M, Fig 7) to a degree much closer than any uncertainty associated with the vector curvature measurement, consistent with the MFL geometry expected from Hall magnetic fields at each encounter near the X-line.

The vector curvature in the L-direction at the current sheet encounter at 20:19:04 UT before the X-line as well as at 20:24:07 UT at the X-line remain distinctly positive after accounting for measurement uncertainty (Fig 17, panel a). This indicates that MMS1 was on the earthward side of the X-line both before and after the low-velocity ion flow reversal at 20:23:09 UT. We believe this contradicts the interpretation by Huang et al. (2018) that the ion flow reversal was associated with a reconnecting X-line passing over MMS, and instead interpret the ion flow reversal as an unrelated event.

In our flapping event we have seen that the ions were not accelerated at all (see Fig 9, panel 2). Huang et al. (2018) argued in favor of electron-only reconnection, such as found recently in the magnetosheath by Phan et al. (2018) where ions do not participate in the process. However, in our case ion jetting is likely absent because the MMS spacecraft cross close to the X-line. Indeed, the TWINS spacecraft saw a region of ion heating, which we discuss next.

In SFig 4 we show observations made by TWINS in the near-tail, using an ion temperature calculation technique described by Keesee et al. (2014). TWINS saw a region of enhanced ion temperatures in the magnetotail lasting about 10 min around the time MMS encountered the EDR. However, it does not appear in the same location as MMS. The line-of-sight mapping used to generate these images assumes a quiet Fairfield model, which does not apply to our situation due to the flapping. Because of that, while we can rely on the TWINS data here to show that there was ion heating, by roughly a factor of two, in the 10 minutes or so surrounding our EDR encounter in the near tail, the location of the ion heating shown by TWINS in these images is likely not accurate. Given that (i) there is quite a bit of tail flapping, and (ii) there was no other other activity observed, the observation by TWINS is likely to related to the same event seen by MMS, and the disagreement in location is probably a projection/mapping issue.

Symmetric reconnection is associated with long current sheets. Adding a density asymmetry, even a small one, shortens them. Our event has a density asymmetry of about $\sim$1.25 (far from the EDR) which, while small, may yet have significant effects. These were discussed by Montag (2018) and Montag et al. (2020), who conducted a study of the impact of small density asymmetries on antiparallel reconnection and concluded that these include a shortening the length of the outflow jets. For long CSs to form, the **B** field lines must bend sharply. This can happen if the magnetic tension force is $\sim$0, i.e., if $P_{\|} - P_{\perp} \sim 2P_B$ (firehose condition). When the magnetic **tension** term in the momentum equation changes sign, the configuration is firehose unstable. CSs can only form when both sides have reached the firehose condition, so that a shortening occurs if this condition is reached first on only one side. Besides, in our case the higher densities occur before the CS is encountered (see Fig 5, panel 3). Montag et al. (2020) showed that trapped electron dynamics cause parallel heating that scales strongly with variation in N, magnifying the rate of parallel heating on each side of the outflow. That is probably the reason why $Te_{\|}$ is higher before the CS is crossed (see Fig 9). The density asymmetry is also accompanied by a small temperature asymmetry (Fig 5, purple trace), and like the density the temperature is also higher before the CS crossing (Fig 5). As the firehose condition scales oppositely with density and temperature this Te-asymmetry tends to weaken the effect of Ne-asymmetry (see Fig 1, Montag et al. 2020). It would be interesting to see what simulations of this event tell us on this issue.

Asymmetries in B and Ne have also an effect on the Hall electromagnetic fields. For example, the electric field normal to the CS, E_N, can even become unipolar and exist only on the low-beta side. This was found in observations and simulations on the dayside and at higher latitudes (Mozer et al., 2008, and references therein; Muzamil et al., 2014, and references therein). Evidently, our asymmetry is not strong enough for the bipolarity to go away. However, on the low-beta side (i.e. after the CS crossing), the E_N is clearly stronger **(Fig 7, third panel)**. **This was also present in the PIC simulations.**

The case we studied was one of asymmetric reconnection with a small guide field. We now compare and contrast with the works of Zhou et al, (2019), who discussed cases of symmetric reconnection in the geomagnetic tail with a small guide field. We note that in the case of Zhou et al. the spacecraft crossed the EDR while going from one side of X-line to the other. Like Zhou et al., we also used the disappearance of the electron temperature anisotropy as a sign that the EDR is being crossed. The temperature anisotropy that is induced by electron trapping in a parallel electric field in the upstream region (Egedal 2013) is thereby removed. For asymmetric reconnection, as we have here, Lavraud et al. (2016) explained the effect in terms of electrons being scattered in phase space while tending to be isotropic near the X-line. The thicknesses of the IDR in the normal direction in the two studies are comparable (0.4 d_i versus 0.55 d_i), while the EDR thickness in our case is three times as much (6 d_e versus 2 d_e). The profiles of the parallel and perpendicular current densities through the IDR are similar: In the EDR, the parallel current dominates in the center and the perpendicular current densities dominate at the edges, forming a shoulder-like **profile**. Zhou et al. argue that the sudden disappearance of parallel electrons within the EDR supports the idea that the magnetic topology there is very different from in the inflow regions. In the IDR the current density is mainly in the perpendicular direction. The reconnection rates, normalized by the inflow magnetic field and Alfvén speed, are however very different in the two studies: **0.27 ± 0.18 (peak value) versus 0.077 ± 0.050 (our average value).**

The observed reconnection rate is in excellent agreement with the steady-state rate from a 2.5-D PIC simulation, as are also the observed and simulated EDR magnetic field, electron velocity, and electron temperature anisotropy profiles. We conclude that the 2.5-D and steady-state approximations are adequate for describing the observed EDR features at the time and location of the crossing. Of course, the reconnection rate will vary during the initial and final phases of a reconnection X-line, hence this caveat. Clearly, 3D structure may be important elsewhere, such as in regions of strong electron-scale turbulence (typically in separatrices or dipolarization fronts, for example).

A number of interesting questions were raised by this study which we have not addressed. The first is that the acceleration of the current sheet resulting from the flapping could affect the reconnection dynamics. This is an interesting point to address in a future analysis of our simulations. The second is the very good agreement that exists between the simulations and the

observations, despite their being of different dimensionality, as has just been mentioned. This agreement seems to imply that, at least approximately, local tail reconnection is not necessarily a fully three-dimensional phenomenon. This was a conclusion reached also by Torbert et al. (2018) in another tail reconnection event. In the interests of brevity and not to overburden the analysis we reserve this topic for future work.

Sergeev et al. (2006) carried out a statistical study of tail flapping events using Geotail observations. Based on a superposed epoch analysis of the auroral AE index, they found that the flapping motions tend to appear during the substorm expansion phase, although a considerable number of events without any electrojet and auroral activity were also observed (see also Runov et al., 2009). By contrast, we find the flapping here to occur during substorm onset.

Acknowledgments

We are very grateful to Per Even Sandholt and Timothy Rogers for helpful discussions. **We thank both referees for their constructive criticisms.** This work is supported by NASA MMS, 80NSSC20K0197, and 80NSSC19K1293 grants. For the simulations employed in this paper, we acknowledge PRACE for awarding us access to MareNostrum at Barcelona Supercomputing Center (BSC), Spain. TKMN was supported by the Austrian Research Fund (FWF): P32175-N27. Level 2 FGM and FPI data are available at the MMS Science Data Center at *lasp.colorado.edu/mms/sdc/public/*. *Wind* magnetic field and plasma data were obtained from NASA's SPDF/CDAWeb. Level 3 electric field data used in this work are available at *http : //mmspubdata.sr.unh.edu/*. IMAGE ground magnetometer data is from the SuperMAG website. Geomagnetic indices are obtained from the OMNI website.

References

Akasofu, S.-I. (1964), The development of the auroral substorm, *Planet.Space Sci. 12*, 273-282. doi:10.1016/0032-0633(64)90151-5

Bowers, K. J., B. J. Albright, L. Yin, B. Bergen, and T. J. T. Kwan (2008), Ultra-high performance three-dimensional electromagnetic relativistic kinetic plasma simulation, *Phys. Plasmas, 15*, 055703.

Büchner, J., and L. M. Zelenyi (1989), Regular and chaotic charged particle motion in magnetotaillike field reversals: 1. Basic theory of trapped motion, *J. Geophys. Res., 94(A9)*, 11,821 11,842, doi:10.1029/JA094iA09p11821

Genestreti, K. J., Nakamura, T. K. M., Nakamura, R., Denton, R. E., Torbert, R. B., Burch, J. L., et al. (2018). How accurately can we measure the reconnection rate E_M for the MMS diffusion region event of 11 July 2017?, *J. of Geophys. Res.: Space Physics, 123*, https://doi.org/10.1029/2018JA025711

Egedal, J., W. Fox, N. Katz, M. Porkolab, M. Øieroset, R. P. Lin, W. Daughton and J. F. Drake (2008), Evidence and theory for trapped electrons in guide field magnetotail reconnection, textitJ. Geophys. Res., 113, A12207, doi:10.1029/2008JA013520.

Egedal, J., A. Le, and W. Daughton (2013), A review of pressure anisotropy caused by electron trapping in collisionless plasma, and its implication for magnetic reconnection, Phys. Plasmas 20, 061201.

Ergun, R., et al. (2016), The Axial Double Probe and Fields Signal Processing for the MMS Mission, *Space Science Revs, 199(1-4)*, 167-188, doi:doi:10.1007/s11214-014-0115x.

Erkaev, N. V., V. S. Semenov, and H. K. Biernat (2008), Magnetic double gradient mechanism for flapping oscillations of a current sheet, Geophys. Res. Lett., 35, L02111, doi:10.1029/2007GL032277.

Fuselier, S.A., Lewis, W.S., Schiff, C. et al. Magnetospheric Multiscale Science Mission Profile and Operations. Space Sci Rev 199, 77103 (2016). https://doi.org/10.1007/s11214-014-0087-x

Henderson, M., S. K Morley, J. Niehof, and B. Larsen (2018), *LANLGeoMag. Zenodo*, doi:10.5281/zenodo.1195041

Huang, S. Y., K. Jiang, Z. G. Yaun, F. Sahroui, L. H. He, M. Zhou, et al. (2018), Observations of the electron jet generated by secondary reconnection in the terrestral magnetotail, *Astrophy. J. 862:144*,doi: 10.3847/1538-4357.

Keesee, A. M. and M. W. Chen and E. E. Scime and A. T. Y. Lui (2014), Regions of ion energization observed during the Galaxy-15 substorm with TWINS, J. Geophys. Res., 119, doi:10.1002/2014JA020466.

Knetter, T., F. M. Neubauer, T. Horbury, and A. Balogh (2004), Four-point discontinuity observations using Cluster magnetic field data: A statistical survey, *J.*

Geophys. Res., 109 A06102, doi:10.1029/2003JA010099.

Lavraud, B., Y. C. Zhang, Y. Vernisse, D. J. Gershman, J. Dorelli, P. A. Cassak, et al. (2016), Currents and associated electron scattering and bouncing near the diffusion region at Earth's magnetopause (2016), *Geophys. Res. Lett., 43,*, 30423050, doi:10.1002/2016GL068359

Le, A., J. Egedal, and W. Daughton (2016), Two-stage bulk electron heating in the diffusion region of anti-parallel symmetric reconnection, Phys. Plasmas 23, 102109.

Le Contel, O., et al. (2016), The Search-Coil Magnetometer for MMS, *Space Science Revs.,199(1-4)*, 257-282, doi:10.1007/s11214-014-0096-9.

Lepping, R.P., Acna, M.H., Burlaga, L.F. et al. (1995), The WIND magnetic field investigation, *Space Sci Rev 71*: 207, doi.org/10.1007/BF00751330

Lin, R. P., et al. (1995), A Three-Dimensional Plasma and Energetic Particle Investigation for the Wind spacecraft, *Space Sci. Rev., 71*, pp. 125, 1995.

Lindqvist, P., et al. (2016), The Spin-Plane Double Probe Electric Field Instrument for MMS, *Space Science Revs., 199(1-4)*, 5635-5643, doi: 10.1007/s11214-014-0116-9.

Lockwood, M, S. W. H. Cowley, and M. P. Freeman (1990), The excitation of plasma convection in the high-latitude ionosphere, *J. Geophys. Res., 95*, A6, 7961-7972.

Lui, A. T. Y., Meng, and S.-J. Akasofu (1978), Wavy nature of the magnetotail current sheet, *Geophys. Res. Lett.,* https://doi.org/10.1029/GL005i004p00279.

P. Montag (2018), Modeling the formation of current sheets in symmetric and asymmetric reconnection, PhD thesis, Massachusetts Institute of Technology, (supervisor: J. Egedal)

Montag, P., J. Egedal, and W. Daughton (2020), Influence of inflow density and temperature asymmetry on the formation of electron jets during magnetic reconnection, *Geophys. Res. Lett.*, https://doi.org/10.1029/2020GL087612.

Mozer, F. S., P. L. Pritchett, J. Bonnell, D. Sundkvist, and M. T. Chang (2008), Observations and simulations of asymmetric magnetic field reconnection, *J. Geophys. Res., 113, A00C03*, doi: 10.1029/2008JA103535.

Muzamil, F., C.J. Farrugia, R.B. Torbert, P. R. Pritchett , F.S. Mozer, J.D. Scudder, P. E. Sandholt , C. T. Russell , W. F Denig, and L. Wilson III (2014), Structure of a reconnection layer poleward of the cusp: Extreme density asymmetry and a guide field, *J. Geophys. Res. Space Physics*, 119, doi:10.1002/2014JA01987.

S. K. Morley (2015), Magnetic ephemeris and coordinates: Level 2n ephemeris product update. Zenodo. doi:10.5281/zenodo.2594027

Nagai, T. et al. (2001), Geotail observations of the Hall current system: Evidence of magnetic reconnection in the magnetotail. *J. Geophys. Res.* **https://doi.org/10.1029/2001JA900038.**

N. F. Ness (1965), The Earth's magnetic tail, *J. Geophys. Res.*, doi:10.1029 JZ070i013p02989.

Phan, T. D., J. P. Eastwood, M. A. Shay, et al., (2018), Electron magnetic reconnection without ion coupling in Earth's turbulent magnetosheath, *Nature, 557*, 202-2-6, htpertps://doi.org/10.1038/s41586-018-0091-5.

Pollock, C., at al. (2016), Fast Plasma Investigation for Magnetospheric Multiscale, *Space Science Revs., 199(1-4)*, 331-406, doi:10.1007/s11214-016-0245-4.

Rogers, A.J., C. J. Farrugia, R. B. and Torbert (2019), Numerical Algorithm for Detecting Ion Diffusion Regions in the Geomagnetic Tail With Applications to MMS Tail Season 1 May to 30 September 2017, *JGR:Space Physics, 124*. doi:10.1029/2018JA026429

Runov, A., R. Nakamura, W. Baumjohann, T. L. Zhang, M. Volwerk, H. U. Eichelberger, and A. Balogh (2003), Cluster observation of a bifurcated current sheet, *Geophys. Res. Lett., 30(2)*, 1036, doi:10.1029/2002GL016136, 2003.

Runov, A., V. A. Sergeev, W. Baumjohann, R. Nakamura, S. Apatenkov, Y. Asano, M. Volwerk, Z. Vörös, T. L. Zhang, A. Petrukovich, A. Balogh, J.-A. Sauvaud, B. Klecker, and H. Rme (2005), Electric current and magnetic field geometry in flapping magnetotail current sheets, *Annales Geophysicae, 23*, 13911403.

Runov, A., V. Angelopoulos, V. A. Sergeev, K.-H. Glassmeier, U. Auster, J. McFadden, D. Larson, and I. Mann (2009), Global properties of magnetotail current sheet flapping: THEMIS perspectives, *Ann. Geophys., 27,* 319-328.

Russell, C. T., M. M. Mellott, E. J. Smith, and J. H. King (1983), Multiple spacecraft observations of interplanetary shocks: Four spacecraft determination of shock normals, *J. Geophys. Res., 88*, 4739 4748, doi:10.1029/JA088iA06p04739.

Russell, C., et al. (2016), The Magnetospheric Multiscale Magnetometers, *Space Science Revs., 199(1-4)*, 189-256, doi:10.1007/s11214-014-0057-3.

Scudder, J. D., R. D. Holdaway, R. Glassberg, and S. L. Rodriguez (2008), Electron diffussion region and thermal demagnetization, *J. Geophys. Res., 113*, A10208, doi:10.1029/2008JA013361.

Sergeev, V. A., A. Runov, M. Baumjohann, R. Nakamura, T. L. Zhang, M. Volwerk, A. Balogh, H. Rème,J. A. Sauvaud, J. A., M. Andrè, and B. Klecker (2003), Current sheet flapping motion and structure observed by Cluster, *Geophys. Res. Lett., 30*, 1327, doi:10.1029/2002GL016500.

Sergeev, V., A. Runov, W. Baumjohann, R. Nakamura, T. L. Zhang, A. Balogh, P. Louarn, J.-A. Sauvaud, and H. Rème (2004), Orientation and propagation of current sheet oscillations, *Geophys. Res. Lett., 31*, L05807, doi:10.1029/2003GL019346.

Sergeev, V. A., D. A. Sormakov, S. V. Apatenkov, W. Baumjohann, R. Nakamura, A. Runov, T. Mukai, and T. Nagai (2006), Survey of large-amplitude flapping motions in the midtail current sheet, *Ann. Geophys., 24*, 20152024.

Sergeev, V. A., N. A. Tsyganenko, and V. Angelopoulos (2008), Dynamical response of the magnetotail to changes of the solar wind direction: an MHD modeling perspective, *Ann. Geophys., 26*, 2395-2402.

Shen, C., X. Li, M. Dunlop, Q. Q. Shi, Z. X. Liu, E. Lucek, and Z. Q. Chen (2007), Magnetic field rotation analysis and the applications, *J. Geophys. Res., 112*, A06211, doi:10.1029/2005JA011584.

Shen, C., Rong, Z.J., Li, X., Dunlop, M., Liu, Z.X., Malova, H.V., et al. (2008), Magnetic configurations of the tilted current sheets in magnetotail. *Ann. Geophys., 26*, 3525-3543. doi:10.5194/angeo-26-3525-2008

Sonnerup, B. U. Ö., and M. Scheible (1998), Minimum and maximum variance analysis, in Analysis Methods for Multispacecraft Data, edited by G. Paschmann and P. W. Daly, chap. 8, pp. 185 220, ESA Publ., Noordwijk, Netherlands.

Speiser, T. W. and N. F. Ness (1967), The neutral sheet in the geomagnetic tail: Its motion, equivalent currents, and field Line connection through it, *J. Geophys. Res., 72*, 131-139.

Toichi, T. and T. Miyazaki (1976), Flapping motions of the tail plasma sheet induced by the interplanetary field variations, *Planet. Space Science, 24*, 147-159, doi:org/10.1016/0032-0633(76)90102-1.

Torbert, R.B., et al. (2016), The FIELDS Instrument Suite on MMS: Scientific Objectives, Measurements, and Data Products, *Space Science Revs., 199(1-4)*, 105-135, doi: 10.1007/s11214-014-0109-9.

Torbert, R. B., J. L. Burch, T. D. Phan, M. Hesse, M. R. Argall, et al. (2018), Electron-scale dynamics of the diffusion region during symmetric magnetic reconnection in space, *Science, 362*, 1391-1395.

Troshichev, O. A., V. G. Andrezen, S. Vennerstrom and E. Friss-Christensen, (1998), Magnetic activity in the polar cap–A new index, *Planet. Space Sci., 31 (11)*, 1095-1102.

Wang, R., Lu, Q., Nakamura, R., Baumjohann, W., Huang, C., Russell, C. T., et al. (2018), An electron-scale current sheet without bursty reconnection signatures observed in the near-Earth tail, *Geophys. Res. Lett., 45*, 45424549. doi:10.1002/2017GL076330

Wang, R., Q. Lu, C. Huang, and S. Wang (2010), Multispacecraft observation of electron pitch angle distributions in magnetotail reconnection, *J. Geophys. Res., 115*, A01209, doi:10.1029/2009JA01455.

Wang, H., Lühr, H., Ma, S.Y., Ritter, P. 2005. "Statistical study of the substorm onset: its dependence on solar wind parameters and solar illumination." Annales Geophysicae. 23. 20692079. doi:10.5194/angeo-23-2069-2005

Zhang, T. L., W. Baumjohann, R. Nakamura, A. Balogh, and K.-H. Glassmeier (2002), A wavy twisted neutral sheet observed by Cluster, *Geophys. Res. Lett., 29(19)*, 1899, doi:10.1029/2002GL015544.

Zhang, T. L., R. Nakamura, M. Volwerk, A. Runov, W. Baumjohann, H. U. Eichelberger, C. Carr, C., A. Balogh, V. Sergeev, J. K. Shi, and K-H. Fornacon (2005), Double Star/Cluster observation of neutral sheet oscillations on 5 August 2004, Ann. Geophys., 23, 29092914. http://www.ann-geophys.net/23/2909/2005/.

Zhou, M., X. H. Deng, Z. H. Zhong, Y. Pnag, R. X. Tang, et al. (2019), Observations of an electron diffusion region in symmetric reconnection with a weak guide field, *ApJ*, 870:34, doi:https://doi.org/10.3847/1438-4357/aaf16f

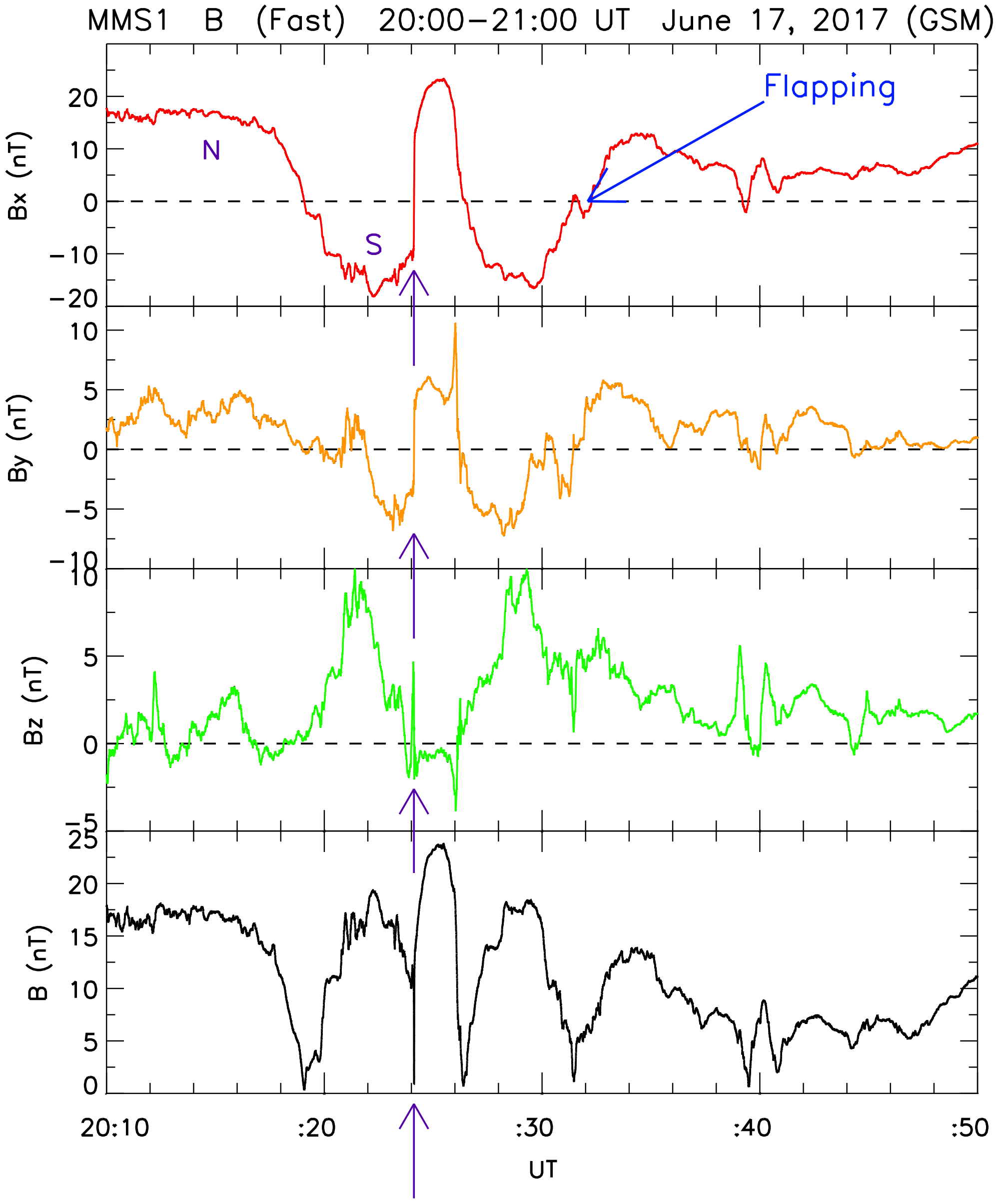

180 **Figure 1.** Magnetic field data from MMS1 for the overview interval 20:10 to 20:50 UT. The
181 data are in survey mode. From top to bottom: the GSM components and the total field strength.

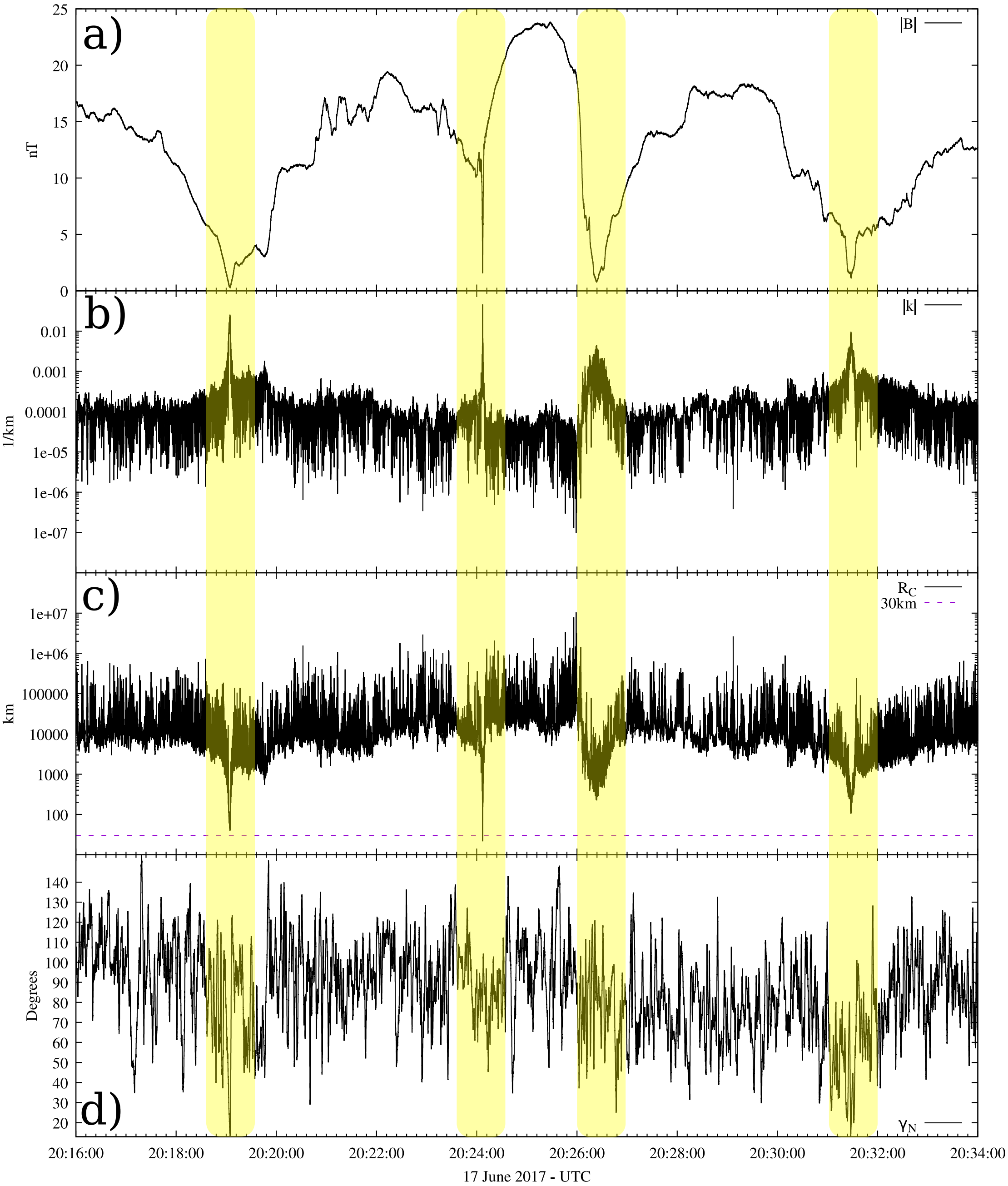

Figure 2. Magnetic Field Line (MFL) geometry parameters for the 18 minutes surrounding the EDR encounter at ~20:24:07 UT on June 17, 2017. Current sheet (CS) encounters during this period are highlighted in yellow and the magnitude of the magnetic field is provided for context (panel a) Parameter $|\mathbf{k}|$ is shown in panel b and is large at each CS crossing. Panel c shows the MFL radius of curvature, where $R_C = |\mathbf{k}|^{-1}$ with the nominal spacecraft separation of MMS during this period shown as a dashed purple line. γ_N (panel d) is the angle between the plane of MFL curvature and the current vector.

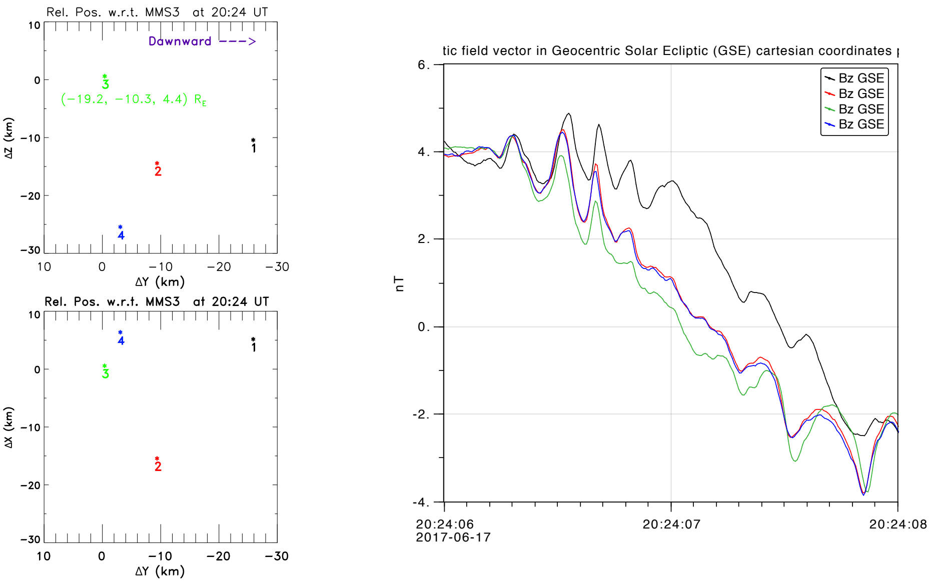

Figure 3. *Left*: The positions of the spacecraft relative to MMS3 at 20:24 UT. GSE coordinates are used. The YZ plane (top) and the YX plane. *Right*: Profiles of B_z (GSE) over a 2 s interval. The temporal order is MMS3 (green) to MMS2/MMS4 (red, blue) to MMS1 (black).

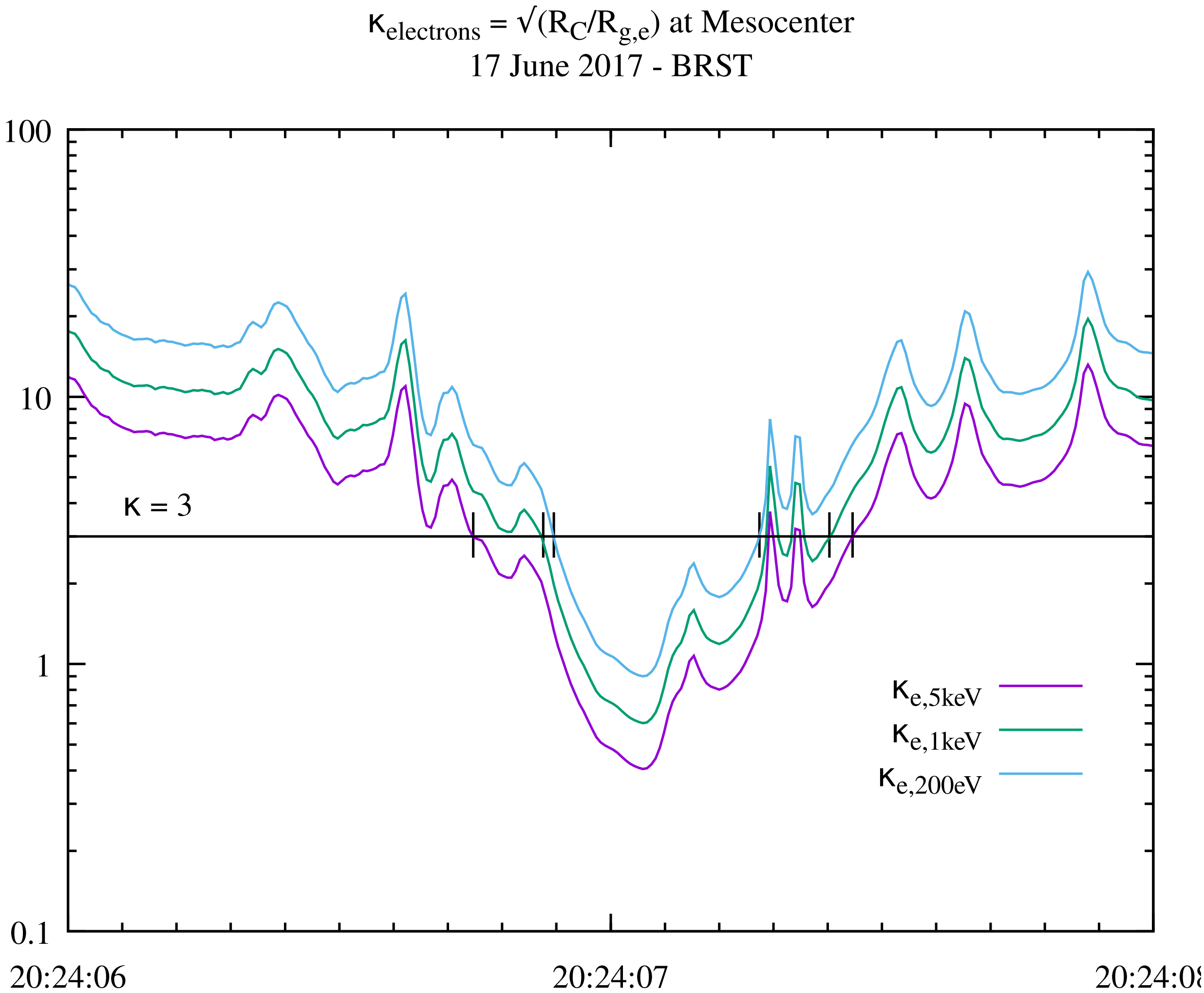

Figure 4. The curvature parameter κ, defined at the top of the figure, calculated at the mesocenter of the spacecraft configuration, for the 3 perpendicular energies of electrons shown at bottom right. For κ less than 10, chaotic behavior, and for κ less than 3 scattering, are expected.

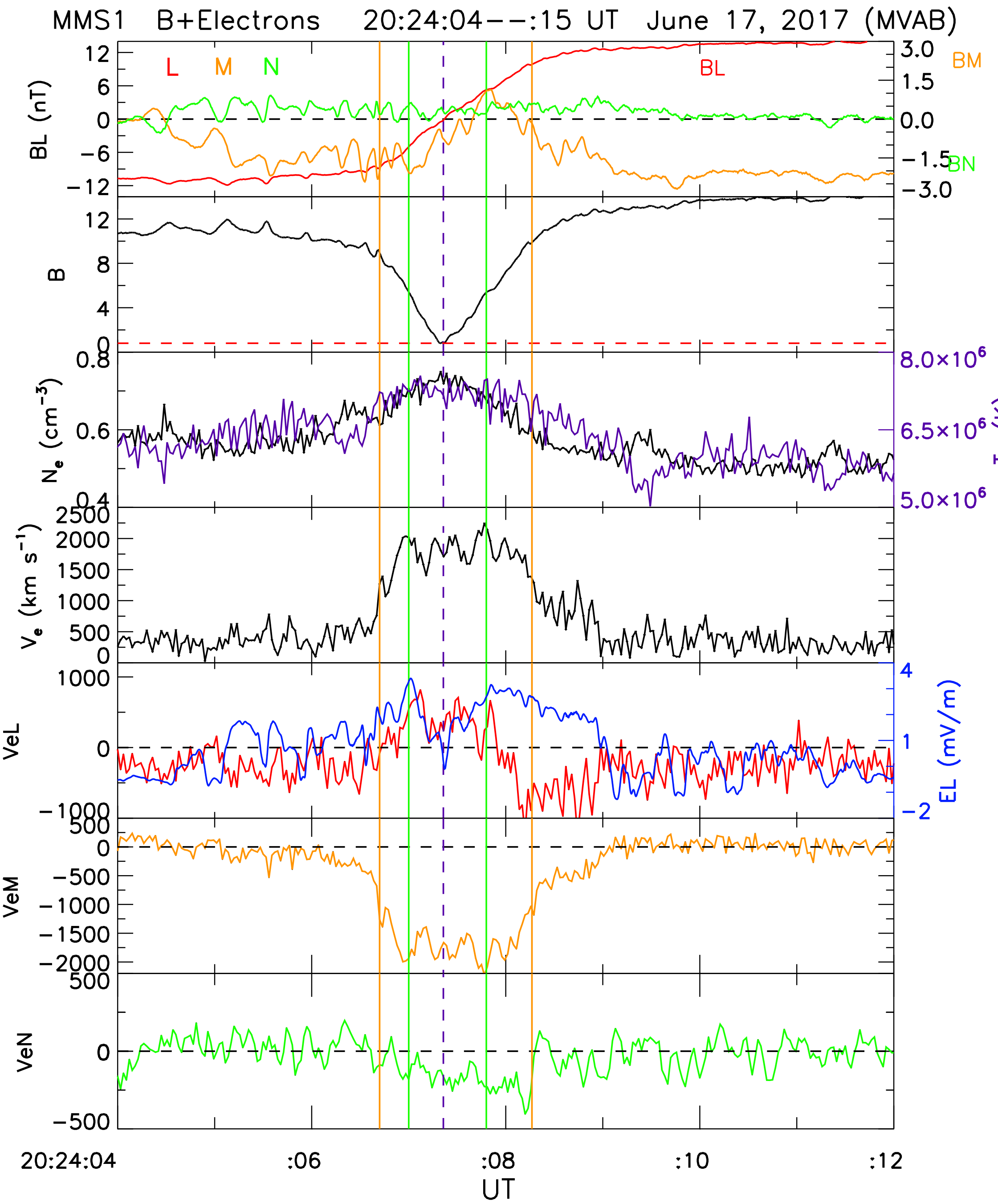

Figure 5. Electron behavior. From top to bottom: the magnetic field in LMN coordinates, the total field strength, the electron density and, overlaid in purple with scale on the right, the electron temperature, the bulk flow speed, and the electron velocity in LMN coordinates. In panel 1 the scale of B_M and B_N is shown on the right. **The dashed horizontal red line in panel 2 shows the size of the guide field**. In the Ve$_L$ panel is overlaid in blue the L-component of the level 3 electric field.

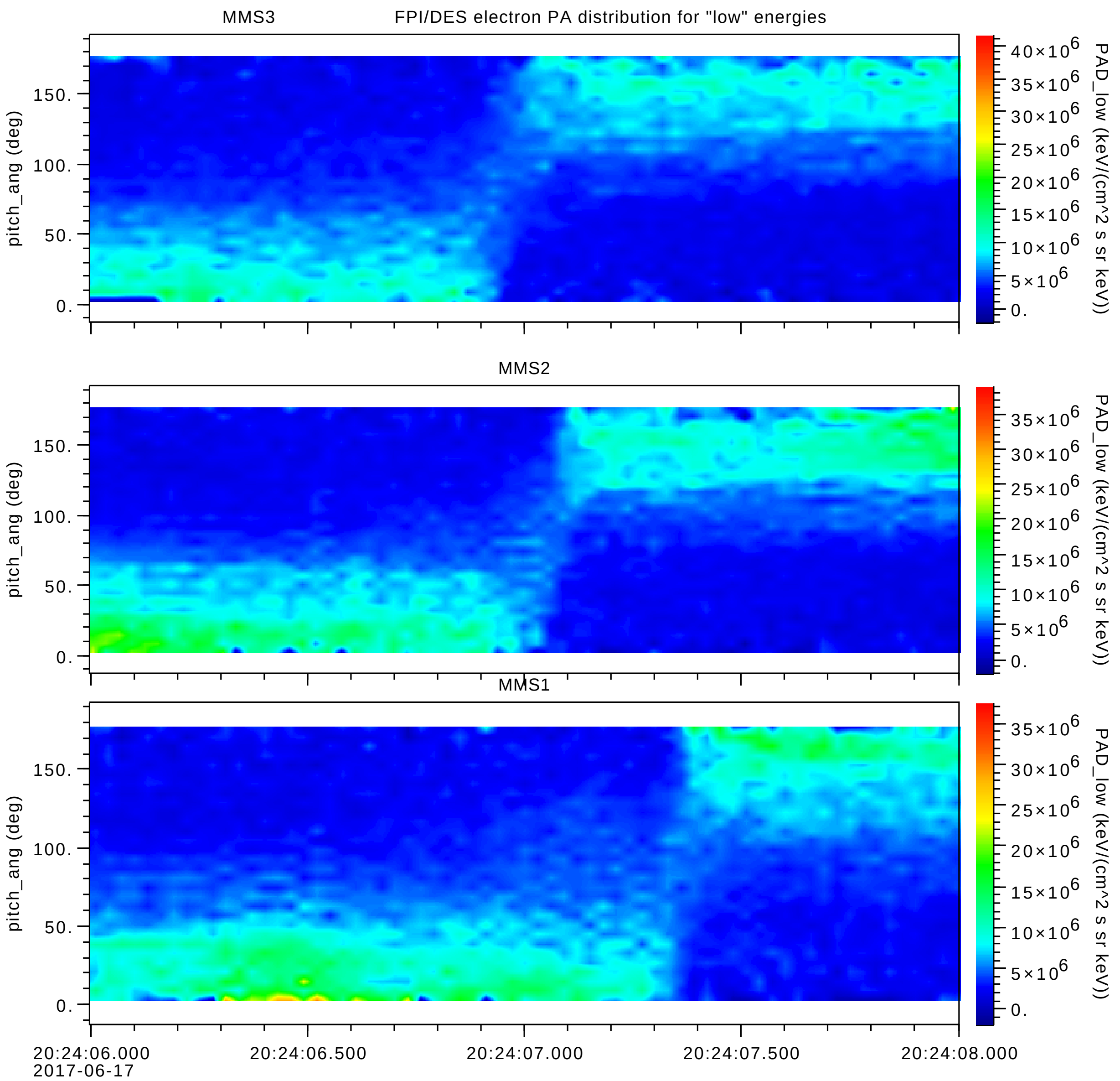

Figure 6. For a 2-s interval centered on the CS crossing, the figure shows the pitch angle distributions of electrons with energies in the range 20-200 eV for, from top to bottom, MMS3, MMS2, and MMS1.

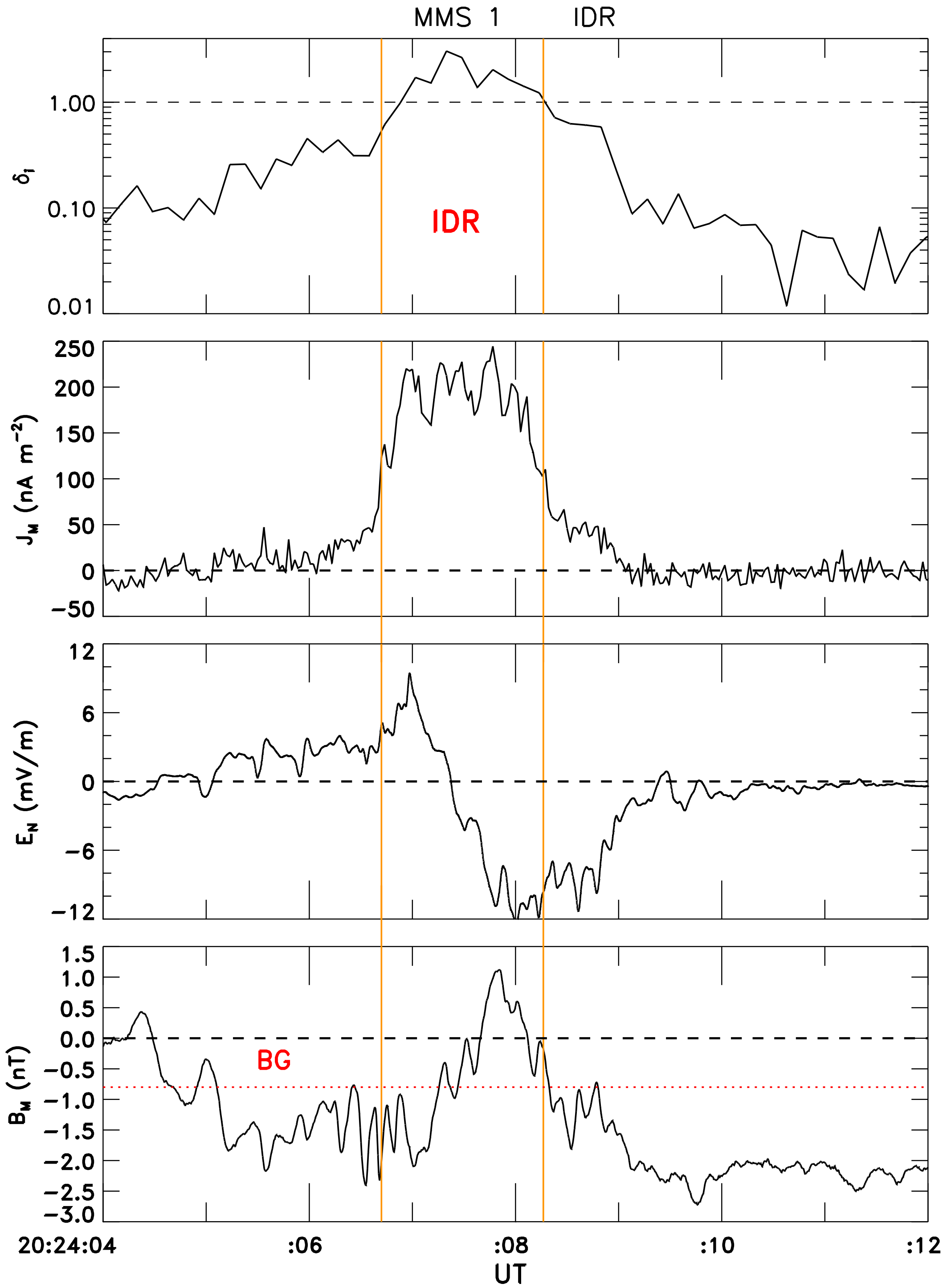

Figure 7. Physical quantities used to identify the ion diffusion region, IDR: the adiabatic expansion parameter, δ_i, the out-of-plane current density, J_M, the (Hall) electric field component normal to the CS, E_N, and the (Hall) out-of-plane magnetic field B_M. The guide field is shown by the horizontal red trace. The orange guidelines bracket the IDR.

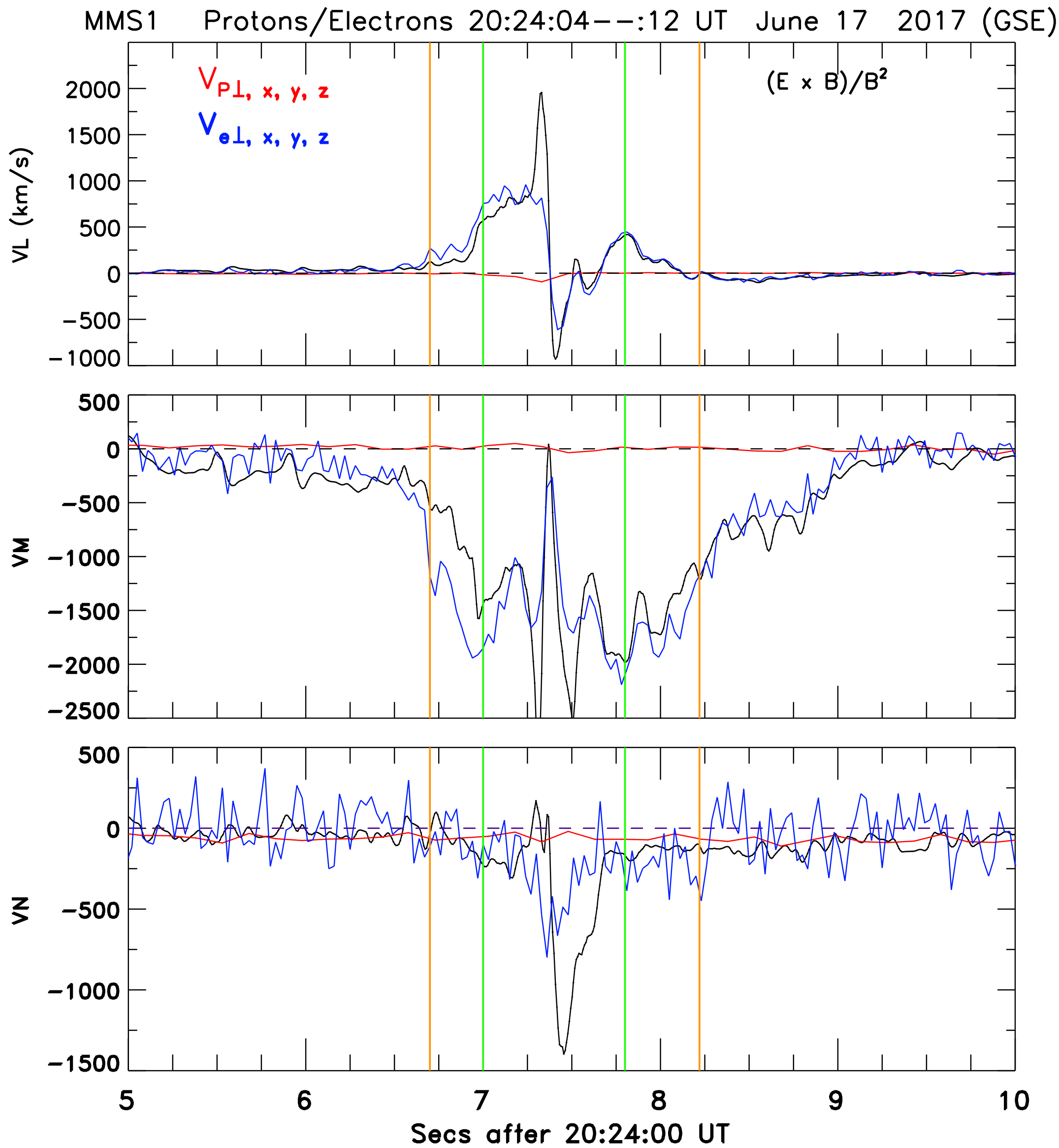

318 **Figure 8. An overlay of the velocity of protons (red) and electrons (blue) perpen-**
319 **dicular to the magnetic field and the $E \times B$ drift velocity in black. The vertical lines**
320 **mark the boundaries of the IDR (magenta) and EDR (green).**

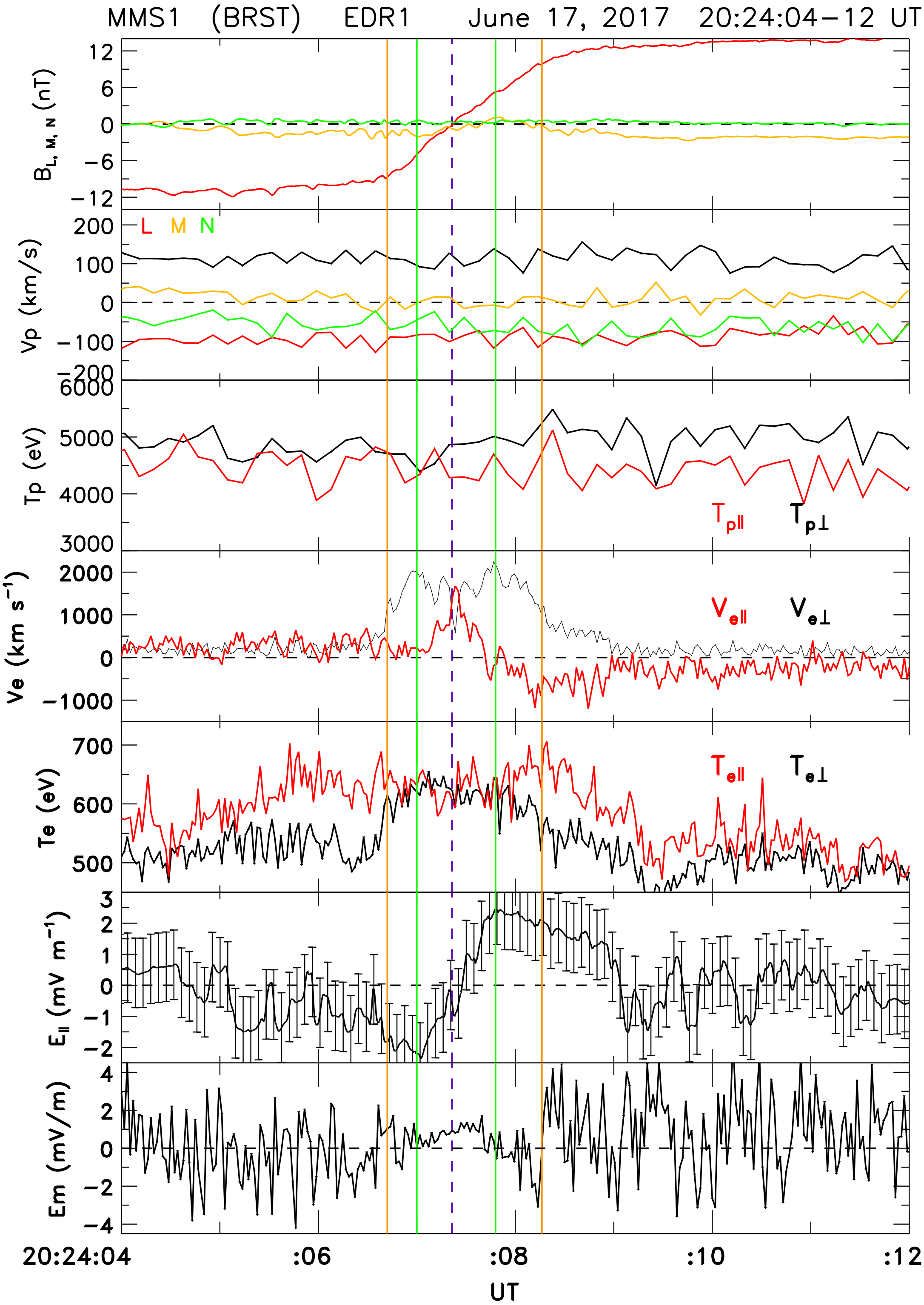

Figure 9. From top to bottom, the panels show: the components of the magnetic field in LMN for reference, the proton bulk velocities, the parallel (red) and perpendicular proton temperatures, the electron velocities parallel (red) and perpendicular to the magnetic field, the parallel (red) and perpendicular electron temperatures, the parallel electric field with error bars included, and the electric field in the out-of-plane direction, E_M.

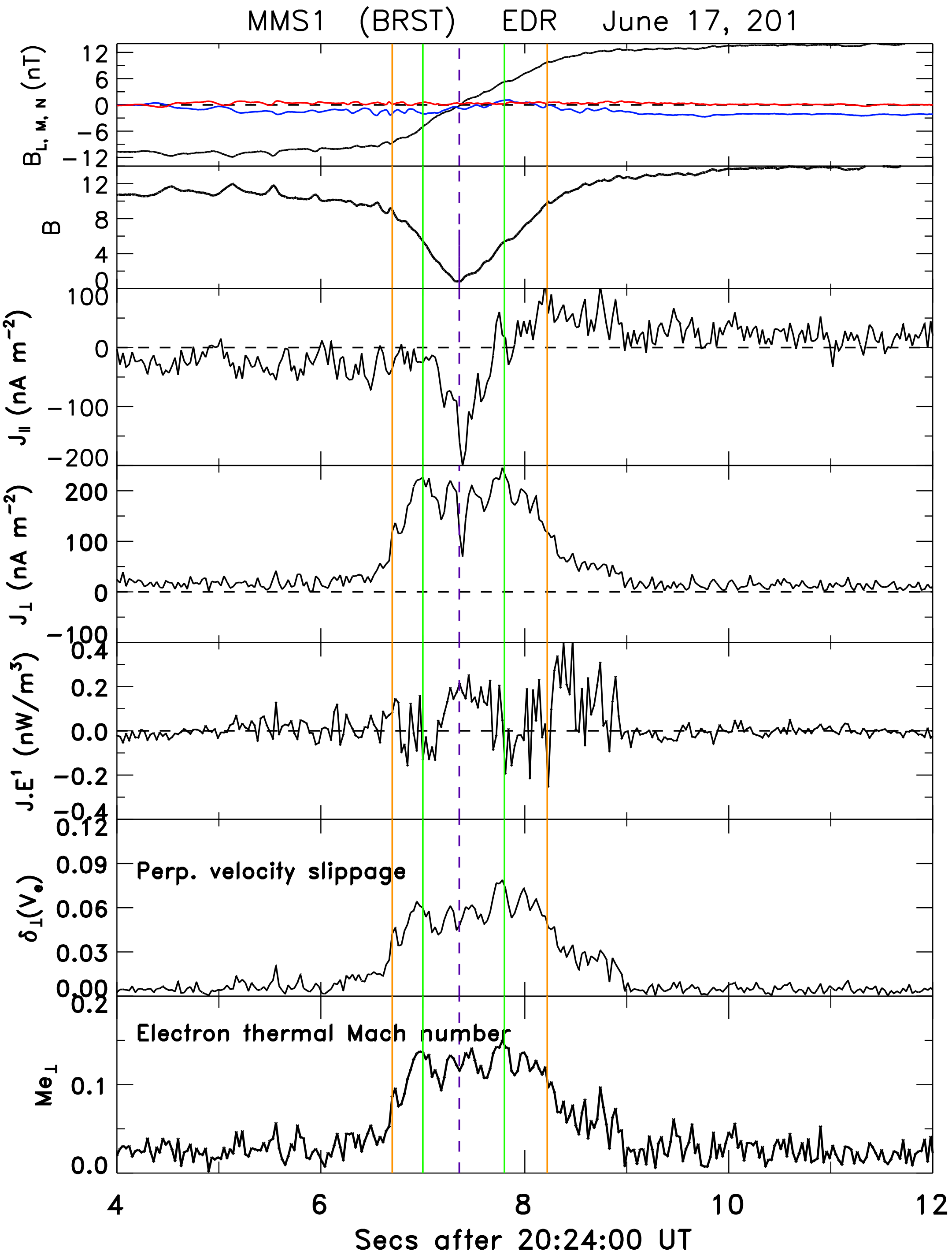

Figure 10. From top to bottom, the panels give the magnetic field components and field strength for reference, the current densities parallel and perpendicular to the magnetic field, the energy transfer term **J.E**', the perpendicular velocity slippage, and the electron thermal Mach number. In the first panel, the B_L, B_M, and B_N are shown by black, blue and red traces, respectively.

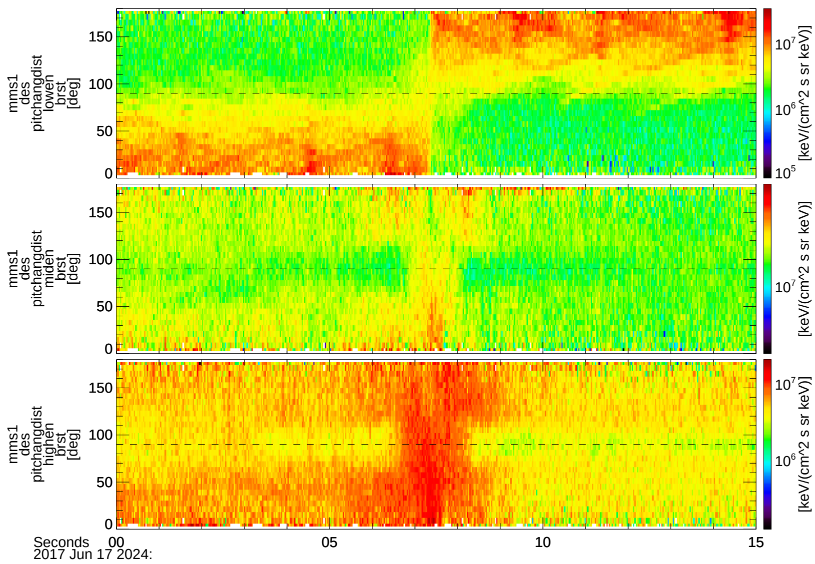

411 **Figure 11.** The PAD distribution of, from top to bottom, low (2-0.200 eV), middle and high energy electrons recorded by MMS1. Note the depletion of anti-parallel mid-energy electrons during the EDR encounter.

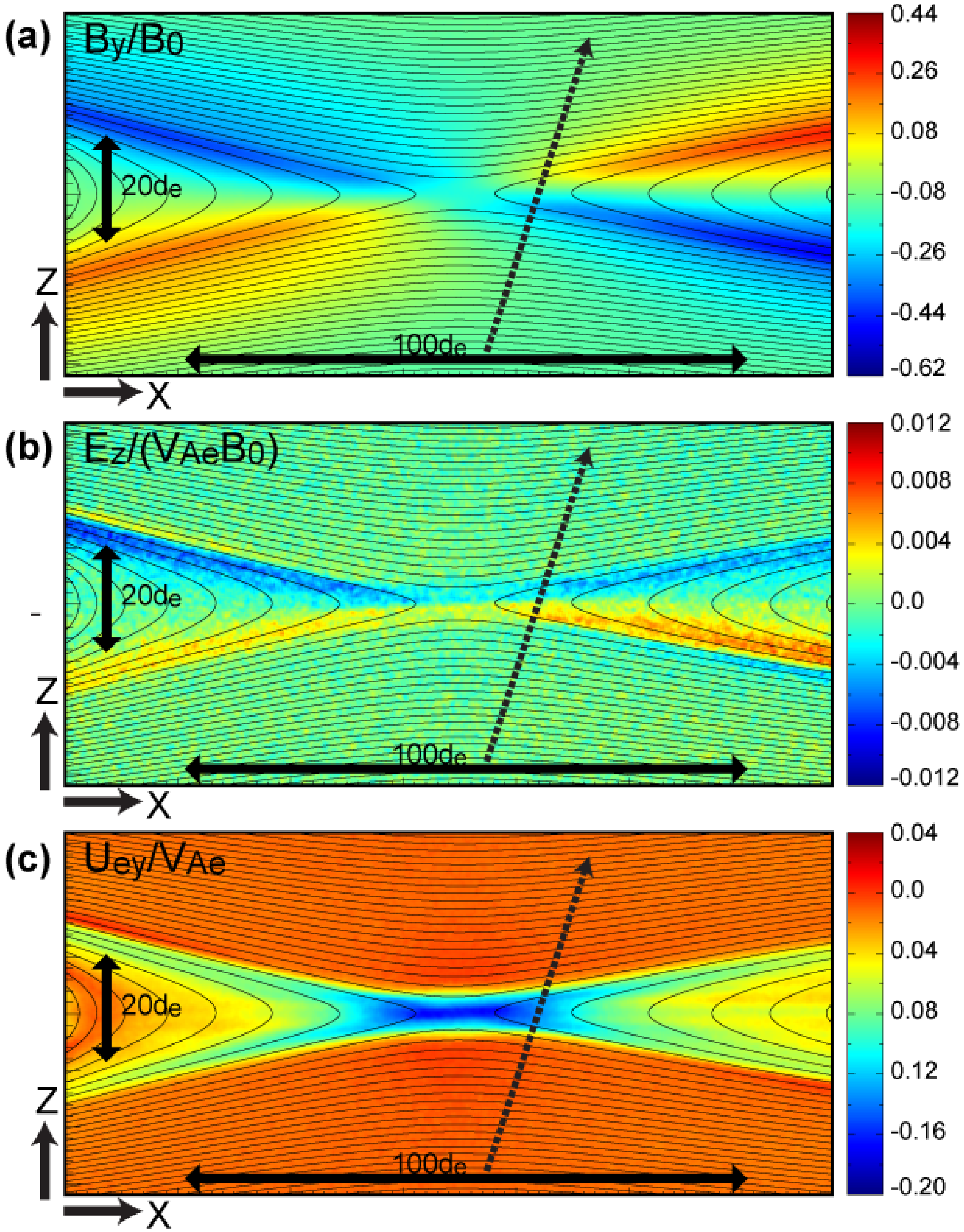

Figure 12. Zoomed-in views of 2-D contours near the IDR at t=45 Ω^{-1}, at which the growth of reconnection is in an almost steady phase, of (a) B_y, (b) E_z, and (c) the electron velocity component U_{ey}, all of which are normalized by B_0, and the electron Alfvén speed V_{Ae} based on B_0 and n_0. The black curves show the in-plane magnetic field lines. The black arrow shows a path of a virtual observation probe. See text for more details on the probe path.

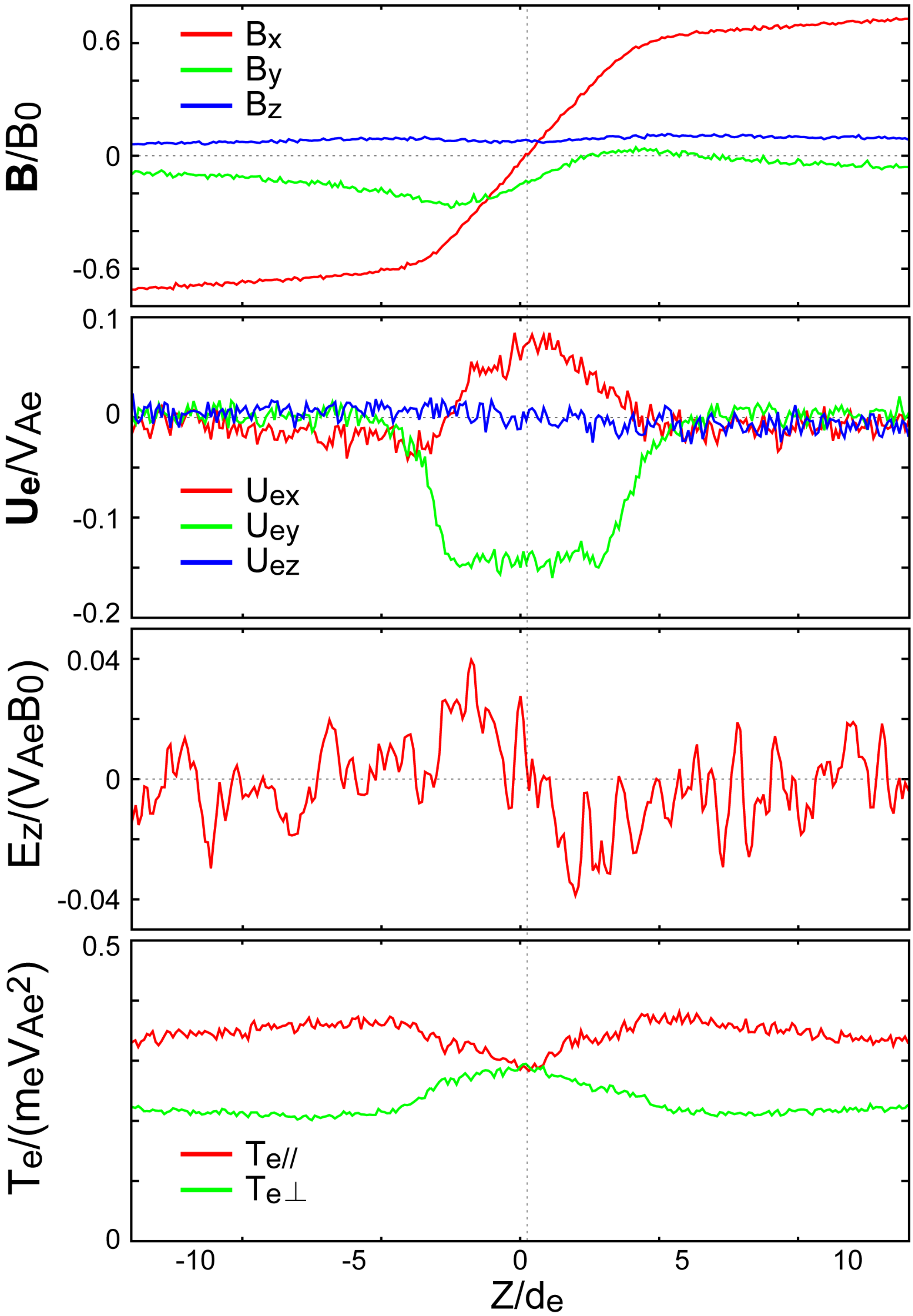

449 **Figure 13.** Virtual observations along the path shown in Fig 12 of (a) the three components
450 of the magnetic field **B**, (b) the three components of the electron bulk velocity U_e , (c) the z
451 component of the electric field E_z , and (d) the parallel ($Te_{\parallel}$) and perpendicular ($Te_{\perp}$) compo-
452 nents of the electron temperature, all of which are normalized by B_0, V_{Ae} and m_e.

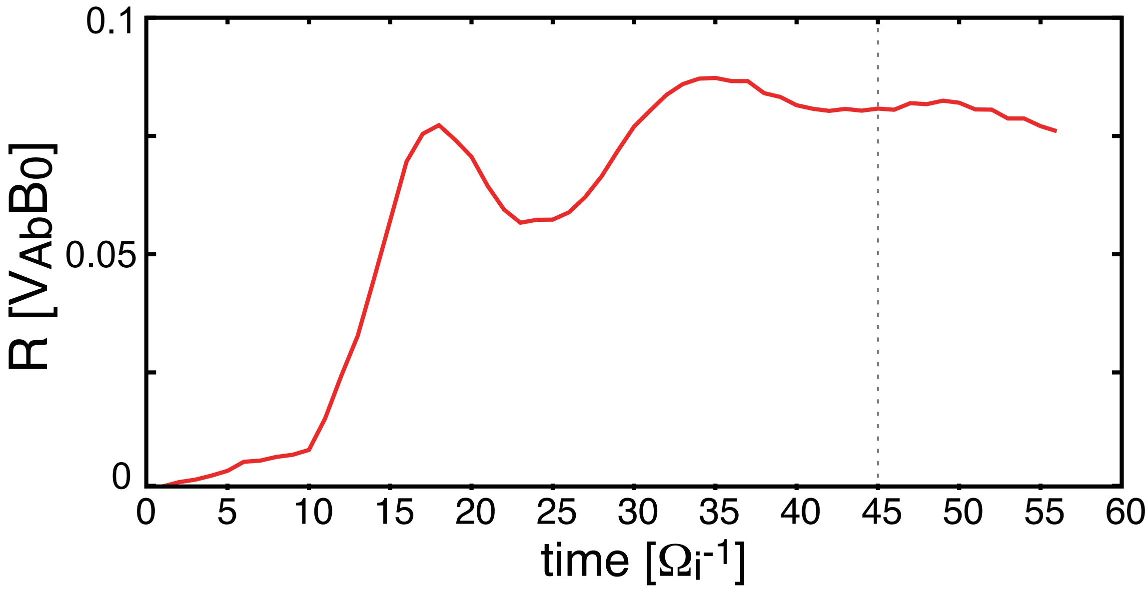

Figure 14. The evolution of the normalized reconnection rate resulting from the simulations.

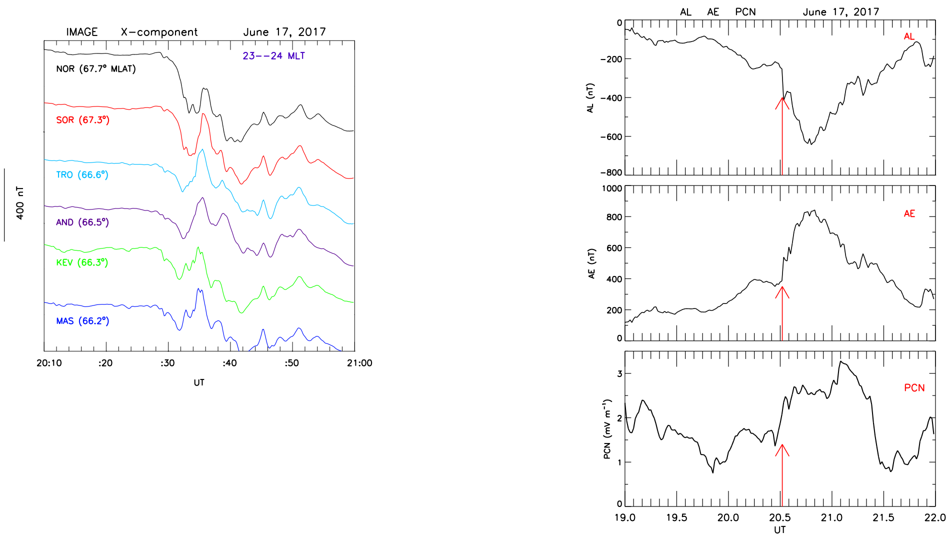

Figure 15. *a (left)*: The north-south (X) component of the geomagnetic field from 6 stations of the IMAGE magnetometer chain at corrected geomagnetic latitudes from 67.7 to 66°. *b (right)*: For the 3-hour interval 19-22 UT, the figure shows the auroral AL and AE indices and the polar cap north index. The time of substorm onset is indicated by the red arrow.

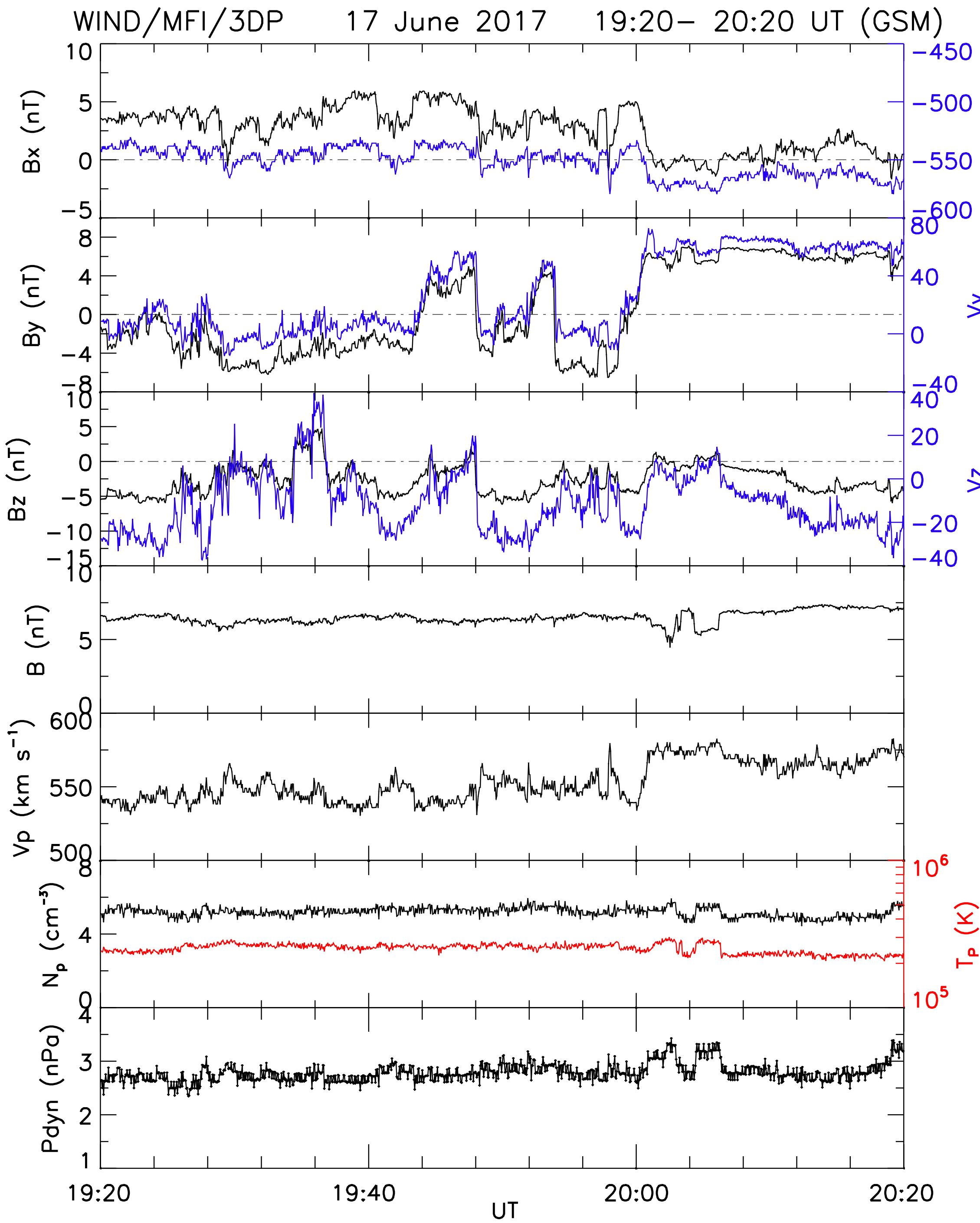

525 **Figure 16.** *Wind* data for a 1-hr interval. From top to bottom, the magnetic field (black) and
526 flow (blue) components, the total field, bulk flow, density and temperature (red) and the dynamic
527 pressure.

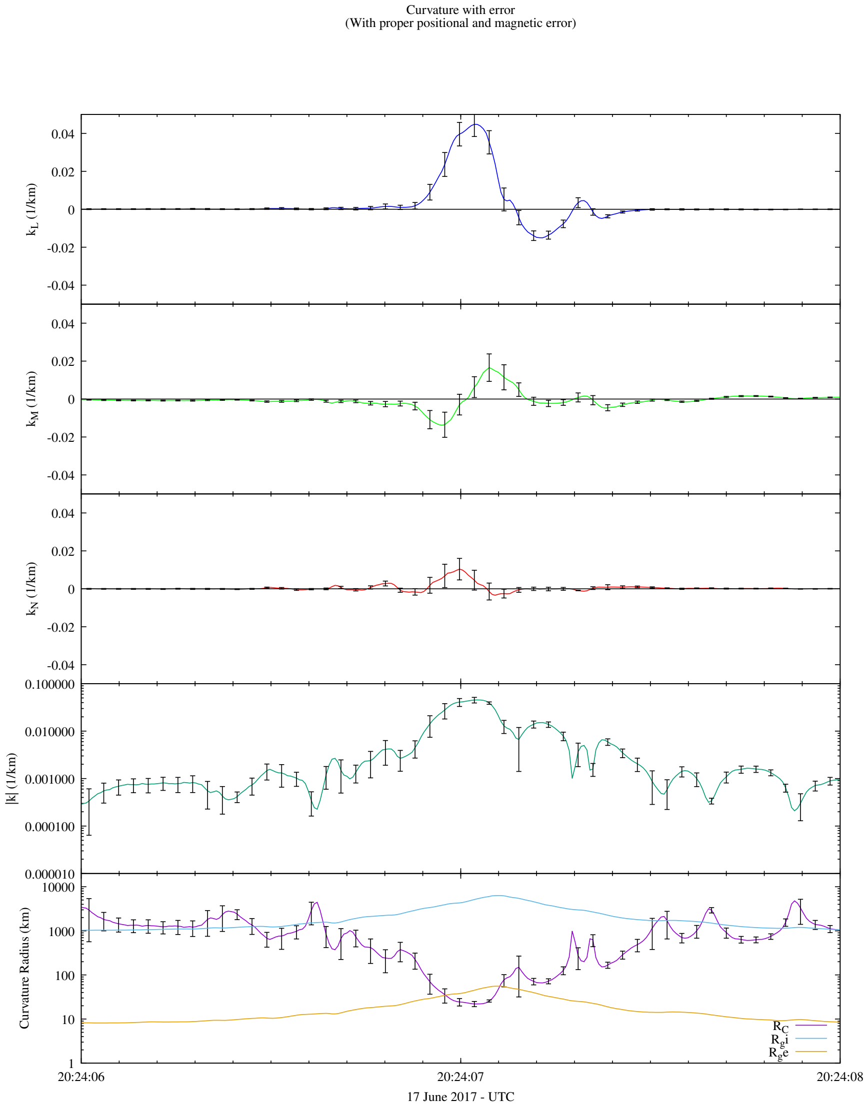

574 **Figure 17.** The components of the magnetic field line (MFL) curvature vector in LMN coordinates, its total value, and the radius of curvature of the MFL, all including uncertainty. Overlaid in the bottom panel are the gyroradii of ions (blue) and electrons (magenta) at their thermal mean energies.